Europa, Ganymede, and Callisto: New Radar Results From Arecibo and Goldstone

S. J. OSTRO,[1] D. B. CAMPBELL,[2] R. A. SIMPSON,[3] R. S. HUDSON,[4] J. F. CHANDLER,[5] K. D. ROSEMA,[1]
I. I. SHAPIRO,[5] E. M. STANDISH,[1] R. WINKLER,[1] D. K. YEOMANS,[1] R. VELEZ,[6] AND R. M. GOLDSTEIN[1]

Observations of the icy Galilean satellites, conducted during 1987-1991 with the Arecibo 13-cm system and the Goldstone 3.5-cm system, yield significant improvements in our knowledge of the satellites' radar properties. Hardly any wavelength dependence is seen for either the total power radar albedo $\hat{\sigma}_T$ or the circular polarization ratio μ_C. For Europa, Ganymede, and Callisto our 13-cm estimates of mean values and rms dispersions are $\hat{\sigma}_T$ = 2.60 ± 0.22, 1.39 ± 0.14, and 0.69 ± 0.06; and μ_C = 1.53 ± 0.03, 1.43 ± 0.06, and 1.17 ± 0.04. Radar albedo features are seen on each satellite. Evidence for μ_C features is lacking, except for indications of a weak hemispheric asymmetry for Callisto. That intersatellite and intrasatellite fractional variations in albedo greatly exceed variations in μ_C is consistent with predictions of coherent backscatter theory and implies that albedo might be a crude indicator of relative silicate abundance. The satellites' albedo distributions overlap. The most prominent radar features are tentatively identified with Galileo Regio and the Valhalla basin. Estimates of echo Doppler frequencies show Callisto to be lagging its ephemeris by 200 ± 50 km.

1. INTRODUCTION

The radar echoes from Europa, Ganymede, and Callisto are extraordinary. It has been known for 15 years that these objects' radar reflectivities dwarf values reported for comets, the Moon, the inner planets, and nonmetallic asteroids. When the radar transmission is circularly polarized, the icy satellites return echoes with the incident handedness preserved, in contrast with the behavior of other targets. At the principal Arecibo wavelength of 13 cm, the circular polarization ratio μ_C, of echo power in the same sense of circular polarization as transmitted (the SC sense) to that in the opposite (OC) sense, exceeds unity for each of the icy Galilean satellites but is only ~0.1 for the Moon and less than 0.4 for most other planetary radar targets. The linear polarization ratio (μ_L = OL/SL) is about one half for all three satellites, again considerably larger than for other targets. The satellites' 13-cm radar albedos increase from Callisto to Ganymede to Europa, whose OC radar reflectivity is the same as that of a metal sphere. Observations of Ganymede at Goldstone in 1977 [Goldstein and Green, 1980] indicated that this object's exotic radar behavior is preserved at 3.5 cm. (Articles reporting radar observations of the satellites are listed in Table 1.)

Most efforts to understand the satellites' radar signatures have focused on the search for an electromagnetic scattering mechanism capable of yielding strong echoes with μ_C greater than unity. The 1978-1989 literature suggested that the satellites' signatures might be understood as being due to

mode-decoupled refraction scattering [Hagfors et al., 1985; Eshleman, 1986a] and/or mode-decoupled, multiple, total-internal reflection [Goldstein and Green, 1980; Eshleman, 1986b] from subsurface variations in refractive index. Ostro and Shoemaker [1990] approached the problem from a geologic perspective and outlined explanations for the satellites' radar signatures that considered regolith formation theory, ice physics, and the refraction-scattering and total-internal-reflection models. They argued that prolonged meteoroid bombardment probably has led to the development on each of the icy satellites of regoliths of fragmental debris somewhat similar in structure and particle size distribution to the regolith on the Moon and that diverse heterogeneities in bulk density and hence refractive index are likely to be found within the icy regoliths. They suggested that a variety of subsurface structures and scattering processes might share responsibility for the strange radar echoes.

Hapke [1990] drew attention to a growing body of literature [e.g., Wolf and Maret, 1985; MacKintosh and John, 1988] on laboratory and theoretical investigation of a phenomenon, called "coherent backscatter" or "weak localization," in which illumination of a weakly absorbing, disordered random medium yields very strong backscattering and μ_C greater than unity. The backscattered intensity is enhanced, and the forward diffusion through the medium is reduced, by constructive interference between fields propagating along identical but time-reversed paths [John, 1991]. The degree of the enhancement depends on the transmitted and received polarizations, because scattering produces a sequence of rotations of the polarization vector. The coherence of reversed paths is largely preserved for scattering into the SC state (or, when linears are transmitted, the SL state) but largely destroyed for scattering into the OC (or OL) state [MacKintosh and John, 1988, 1989]. MacKintosh et al. [1989] and Hapke and Blewett [1991] described laboratory experiments that demonstrate the "circular polarization memory" of coherently backscattered light.

Most recently, Peters [1992] has developed a theory for coherent backscatter of vector waves that accounts for effects of polarization and absorption and that can explain the Galilean satellite echoes if the scatterers in the regoliths are anisotropic. Absorption reduces both μ_C and the albedo, the latter dramatically.

One issue that has arisen frequently in discussions of the icy satellites' echoes is the relative importance of long path length

[1]Jet Propulsion Laboratory, California Institute of Technology, Pasadena.

[2]National Astronomy and Ionosphere Center, Cornell University, Ithaca, New York.

[3]Center for Radar Astronomy, Stanford University, Stanford, California.

[4]School of Electrical Engineering and Computer Science, Washington State University, Pullman.

[5]Harvard-Smithsonian Center for Astrophysics, Cambridge, Massachusetts.

TABLE 1. Previously Reported Radar Observations of the Icy Galilean Satellites

Observation Date	Target(s)	Observatory	λ, cm	Reference
1974	GAN	Goldstone	3.5	*Goldstein and Morris* [1975]
1975	EUR, GAN, CAL	Arecibo	13	*Campbell et al.* [1977]
1976	EUR, GAN, CAL	Arecibo	13	*Campbell et al.* [1978]
1977	GAN	Goldstone	3.5	*Goldstein and Green* [1980]
1977-1979	EUR, GAN, CAL	Arecibo	13	*Ostro et al.* [1980]

These results were reviewed by *Ostro* [1982].

in icy materials versus structure that may develop in icy regoliths but not in silicate regoliths. *Ostro and Shoemaker* [1990] suggested that the simplest hypothesis is that the icy regoliths are structurally nearly identical to the lunar regolith and that the exotic echoes from the satellites arise because of extremely long photon path lengths that allow multiple, helicity-preserving scattering events from a wide variety of heterogeneities. Laboratory experiments on scattering from disordered random media [e.g., *Hapke and Blewett*, 1991] support the view that exotic structures are unnecessary.

The satellites' detailed regolith characteristics may not be discernible without in situ subsurface observations. Meanwhile, radar observations can constrain the gross structural characteristics and silicate/ice ratios within the icy satellites' regoliths. It is desirable to determine the degree to which radar albedo and circular polarization ratio are correlated with geologic units, because intersatellite and intrasatellite variations in radar properties presumably are attributable to differences in resurfacing history, cratering history, subsurface thermal history, local surface ablation rate, and/or impurity content of the ice, that is, phenomena whose surficial manifestations let us define geologic units [*McKinnon and Parmentier*, 1986; *Ostro and Shoemaker*, 1990].

Recent observations suggest that echoes from the Mars residual south polar ice cap [*Muhleman et al.*, 1991; *Butler et al.*, 1989], portions of Titan [*Muhleman et al.*, 1990], and even polar caps on Mercury [*Slade et al.*, 1991; *Harmon and Slade*, 1991] resemble those from the icy Galilean satellites. Perhaps icy terrains with high radar albedos and μ_C greater than unity are common in the solar system. These considerations further motivate efforts to document, as accurately and completely as possible, the radar properties of Europa, Ganymede, and Callisto.

The purpose of this paper is to report results of Arecibo and Goldstone radar observations of Europa, Ganymede, and Callisto during 1987-1991. Our Arecibo (2380-MHz, 13-cm) observations used a radar system about 3 times more sensitive than any available during Jupiter's previous passage (1975-1979) through the northern declinations accessible to Arecibo, and our Goldstone (8495-MHz, 3.5-cm) observations used a system about as sensitive as Arecibo was in the late 1970s; see Table 1. The objectives of our observations were to (1) determine the satellites' radar albedos, polarization ratios, and angular scattering laws as functions of wavelength and rotation phase; (2) search for albedo features and polarization features in the echo spectra and determine the surface locations of those features; and (3) measure echo Doppler frequencies to refine our knowledge of the satellites' orbits. Section 2 describes how we made the observations and how we reduced the data to single-date, dual-polarization power spectra. Section 3 describes how we analyzed those spectra. Section 4 discusses the disk-integrated measurements and presents statistics that summarize those results. Section 5, which is devoted to disk-resolved results, discusses evidence for radar features on the satellites and presents radar albedo maps that, albeit crude, permit inferences about the relationship between radar features

and geologic features. Section 6 summarizes our conclusions.

2. OBSERVATIONS AND DATA REDUCTION

Observing procedures at Arecibo and Goldstone were fundamentally similar. Each "run" consisted of transmission of a highly monochromatic, continuous wave (CW) signal for a duration close to the roundtrip light time (typically about 1.2 hours; see Table 2) between the radar and the target, i.e., until the first echoes were about to return, followed by reception of echoes for a similar duration.

TABLE 2. Jupiter's Declination, Distance, and Roundtrip Time Delay (RTT) for Dates Spanning Radar Observations During the 1987-1991 Oppositions

Date	Declination	Distance, AU	RTT, hours
June 21, 1987	8.3°	5.30	1.47
Sept. 1, 1987	9.9°	4.25	1.18
Oct. 15, 1987	8.3°	3.96	1.10
Dec. 6, 1987	6.5°	4.32	1.20
Sept. 10, 1988	20.3°	4.68	1.30
Oct. 23, 1988	20.1°	4.17	1.16
Dec. 8, 1988	19.0°	4.08	1.13
Nov. 27, 1989	22.9°	4.31	1.19
Dec. 20, 1989	23.1°	4.17	1.16
Jan. 13, 1990	23.3°	4.22	1.17
Dec. 11, 1990	17.3°	4.64	1.29
Jan. 10, 1991	18.2°	4.36	1.21
Feb. 8, 1991	19.2	4.33	1.20

TABLE 3. Physical Data for the Icy Galilean Satellites

	Europa	Ganymede	Callisto
Orbit semimajor axis	9.4	15	26
Synodic period, days	3.551	7.155	16.69
Δφ/hour	4.2°	2.1°	0.9°
Diameter D, km	3138	5262	4800
Bandwidth B, Hz			
At 2380 MHz (λ = 13 cm)	1020	849	332
At 8495 MHz (λ = 3.5 cm)	3642	3031	1815

The semimajor axis is in units of Jupiter's radius. The synodic period is measured between superior geocentric conjunctions with Jupiter. φ is the rotation/orbital phase. The limb-to-limb echo bandwidth is B = 4πD/λP. From *Burns* [1986].

TABLE 4. Arecibo Observations of Europa, Ganymede, and Callisto

Target	UTC Date	Start - Stop Time Time	UTC Mean t_0	Phase (ϕ)	Doppler Frequency for 2380-MHz Transmission, Hz
EUR	Oct. 11, 1987	0503 - 0543	0520	40°	188,747 ± 14
EUR	Oct. 14, 1987	0435 - 0538	0503	343°	-38,072 ± 26
EUR	Oct. 16, 1987	0422 - 0507	0447	185°	-298 ± 26
EUR	Oct. 20, 1987	0405 - 0504	0431	230°	-186,576 ± 16
EUR	Nov. 23, 1988	0427 - 0509	0447	64°	180,435 ± 20
EUR	Dec. 1, 1988	0351 - 0433	0412	154°	20,076 ± 23
EUR	Dec. 2, 1988	0346 - 0428	0407	255°	-300,720 ± 20
EUR	Nov. 30, 1989	0627 - 0738	0701	306°	33,999 ± 17
EUR	Dec. 23, 1989	0448 - 0556	0520	113°	227,154 ± 16
EUR	Dec. 26, 1989	0428 - 0531	0503	57°	183,476 ± 18
EUR	Jan. 10, 1990	0319 - 0424	0354	135°	28,949 ± 14
GAN	June 24, 1987	1208 - 1306	1230	82°	558,489 ± 41
GAN	Sept. 3, 1987	0727 - 0838	0759	41°	427,767 ± 8
GAN	Sept. 4, 1987	0723 - 0833	0755	91°	483,081 ± 6
GAN	Oct. 19, 1987	0409 - 0513	0438	193°	-53,340 ± 11
GAN	Nov. 24, 1988	0422 - 0503	0442	224°	-143,340 ± 10
GAN	Nov. 29, 1988	0401 - 0443	0421	116°	91,296 ± 10
GAN	Nov. 30, 1988	0356 - 0438	0416	166°	-32,110 ± 15
GAN	Dec. 3, 1988	0342 - 0424	0402	317°	-215,278 ± 10
GAN	Dec. 24, 1989	0449 - 0558	0518	266°	-153,612 ± 12
GAN	Dec. 27, 1989	0421 - 0530	0457	56°	137,037 ± 7
GAN	Dec. 31, 1989	0427 - 0532	0450	258°	-211,849 ± 6
GAN	Jan. 9, 1990	0325 - 0423	0357	350°	-148,226 ± 10
GAN	Jan. 12, 1990	0313 - 0418	0347	141°	-35,233 ± 6
GAN	Jan. 8, 1991	0625 - 0714	0649	275°	-2,468 ± 7
GAN	Jan. 10, 1991	0628 - 0705	0645	15°	199,984 ± 17
CAL	June 21, 1987	1219 - 1312	1240	324°	304,456 ± 15
CAL	June 25, 1987	1215 - 1300	1232	50°	488,942 ± 15
CAL	Sept. 2, 1987	0733 - 0843	0804	90°	450,083 ± 6
CAL	Oct. 10, 1987	0451 - 0554	0519	191°	38,662 ± 6
CAL	Oct. 22, 1987	0403 - 0507	0428	91°	90,865 ± 6
CAL	Dec. 2, 1987	0106 - 0206	0130	256°	-461,785 ± 15
CAL	Dec. 3, 1987	0106 - 0200	0127	278°	-470,196 ± 14
CAL	Dec. 5, 1987	0056 - 0150	0118	321°	-433,339 ± 15
CAL	Dec. 6, 1987	0052 - 0145	0114	343°	-394,739 ± 15
CAL	Sept. 10, 1988	0919 - 1037	0957	203°	360,960 ± 15
CAL	Sept. 26, 1988	0820 - 0933	0858	187°	357,388 ± 8
CAL	Sept. 27, 1988	0813 - 0926	0850	209°	307,334 ± 9
CAL	Sept. 28, 1988	0806 - 0918	0845	230°	265,095 ± 16
CAL	Nov. 27, 1988	0408 - 0450	0428	86°	82,431 ± 6
CAL	Dec. 4, 1988	0338 - 0419	0358	238°	-216,548 ± 11
CAL	Dec. 5, 1988	0352 - 0415	0402	259°	-244,548 ± 9
CAL	Nov. 27, 1989	0643 - 0752	0716	3°	240,850 ± 12
CAL	Dec. 2, 1989	0617 - 0704	0645	111°	321,968 ± 7
CAL	Jan. 5, 1990	0342 - 0446	0417	126°	21,307 ± 6
CAL	Jan. 13, 1990	0312 - 0415	0343	300°	-266,921 ± 6
CAL	Jan. 11, 1991	0613 - 0700	0639	175°	159,254 ± 10
CAL	Feb. 6, 1991	0417 - 0505	0440	17°	-38,392 ± 6
CAL	Feb. 7, 1991	0413 - 0501	0436	39°	-4,149 ± 7
CAL	Feb. 8, 1991	0408 - 0457	0431	61°	19,042 ± 7

Observations are listed chronologically. We give the start and stop times (hhmm) of data reception, the weighted mean time of data reception t_0, and the weighted mean phase; the weights were $(\Delta x)^{-2}$, with Δx the radar cross section equivalent of the receiver noise. We also give estimates of echo Doppler frequencies $f_{COM}(t_0)$, as discussed in the text. Epochs are referred to the instant of reception at the telescope reference point, which for Arecibo is the center of curvature of the telescope's main reflector. Estimation of Doppler frequencies and associated uncertainties is discussed in the text.

The target's apparent radial motion introduced a continuously changing Doppler shift into the echoes. We avoided spectral smear by tuning the receiver according to an ephemeris generated from prior estimates of the target satellite's orbit about Jupiter, the orbits of Jupiter and the Earth about the solar system's barycenter, and the rotation of the Earth.

Let $f_{COM}(t)$ denote the Doppler frequency shift of hypothet-

ical echoes from the target's center of mass (COM) that are received at the telescope's reference point at UTC epoch t, and let $f_{EPH}(t)$ denote the ephemeris prediction of $f_{COM}(t)$. For our observations, we can treat the offset $f_0(t) = f_{COM}(t) - f_{EPH}(t)$ as constant over the relevant measurement time scales (one to eight hours).

We used two virtually identical receiver channels to receive

TABLE 5. Goldstone Observations of Europa, Ganymede, and Callisto

Target	UTC Date	Runs	Start - Stop Time Time	UTC Mean t_0	Phase (ϕ)	Doppler Frequency for 8495-MHz Transmission, Hz
EUR	Nov. 11, 1988	2	0559 - 0951	0750	299°	-373,080 ± 160
EUR	Nov. 15, 1988	2	0354 - 0702	0530	335°	-127,210 ± 210
EUR	Nov. 16, 1988	2	0623 - 0929	0800	87°	937,500 ± 360
EUR	Nov. 30, 1988	1	0727 - 0833	0800	68°	445,660 ± 190
EUR	Dec. 20, 1989	2	0610 - 0941	0750	179°	214,770 ± 270
EUR	Dec. 24, 1989	2	0611 - 0940	0750	226°	-476,240 ± 160
EUR	Dec. 27, 1990	2	0636 - 1025	0830	57°	1,590,880 ± 210
GAN	Nov. 10, 1988	1	0844 - 0950	0920	248°	-231,160 ± 80
GAN	Nov. 13, 1988	2	0938 - 1235	1030	42°	654,170 ± 100
GAN	Nov. 22, 1988	1	1155 - 1301	1220	140°	357,600 ± 100
GAN	Nov. 29, 1988	2	0335 - 0706	0510	118°	328,810 ± 60
GAN	Dec. 13, 1989	2	0657 - 1028	0840	78°	1,006,650 ± 60
GAN	Dec. 18, 1989	2	0659 - 1029	0900	331°	-49,830 ± 80
GAN	Dec. 29, 1989	2	0540 - 0909	0710	162°	104,350 ± 70
GAN	Dec. 18, 1990	1	0847 - 1001	0920	301°	601,386 ± 180
CAL	Nov. 10, 1988	1	1128 - 1235	1200	84°	786,890 ± 50
CAL	Nov. 26, 1988	2	0504 - 0805	0620	66°	290,340 ± 40
CAL	Dec. 5, 1988	2	0239 - 0602	0420	260°	-858,970 ± 40
CAL	Dec. 8, 1988	4	0243 - 1057	0650	327°	-762,170 ± 30
CAL	Dec. 14, 1989	2	0656 - 1027	0840	13°	472,750 ± 40
CAL	Dec. 15, 1989	2	0744 - 1114	0940	35°	601,620 ± 40
CAL	Dec. 19, 1989	2	0628 - 0939	0810	121°	627,450 ± 50
CAL	Dec. 22, 1989	1	0618 - 0727	0650	185°	107,270 ± 80
CAL	Dec. 27, 1989	2	0551 - 0919	0730	294°	-455,210 ± 40
CAL	Dec. 13, 1990	1	0918 - 1034	0950	270°	751,310 ± 130
CAL	Dec. 22, 1990	1	0815 - 0930	0850	104°	1,497,680 ± 70

Observations are listed chronologically. We give the number of runs, the start and stop times of data reception, the weighted mean time of data reception (t_0, rounded to the nearest 10 min), and the weighted mean phase; the weights were $(\Delta x)^{-2}$, with Δx the radar cross section equivalent of the receiver noise. We also give estimates of echo Doppler frequencies $f_{COM}(t_0)$, as discussed in the text. Epochs are referred to the instant of reception at the telescope reference point, which for Goldstone is the top of the antenna cone. Estimation of Doppler frequencies and associated uncertainties is discussed in the text. Goldstone observations of Callisto in 1987 used a system that was not as sensitive or as well calibrated as the one used during 1988-1990; we do not discuss those observations in this paper.

signals in the OC and SC polarizations simultaneously. Arecibo's short hour-angle window ($\leq$ 2.8 hours) permitted only a single run on each date, but two or more consecutive runs were carried out on most Goldstone dates. For many of the multirun Goldstone dates, receiver channels (1,2) were set to receive (OC,SC) signals during the first run, then (SC,OC) during the second run, (OC,SC) during the third run, and so forth, to help to eliminate systematic errors in the relative calibration of the two channels.

Typical Arecibo radar system parameters during our observations were: transmitter power P_T, 430 kW; system temperature T_S, 33 K for zenith angles Z less than 10°, increasing almost linearly to about 80 K at Z equal to 20°; and one-way antenna gain G, $10^{7.1}$ for Z less than 10°, decreasing to about $10^{6.9}$ at Z equal to 20°. Typical Goldstone parameters were P_T = 360 kW; T_S = 18 K at zenith, increasing to about 25 K at Z equal to 70°; and G = $10^{7.4}$ for Z less than or equal to 70°. For each instrument, we used models of the Z dependence of T_S and G derived from extensive series of drift scans on point radio sources for which reliable flux densities are available. (Similar data are routinely used to maintain antenna pointing models.)

Each instrument's antenna beam is about 2 arc min wide at half maximum, i.e., about twice Jupiter's angular diameter at opposition. Jupiter is a strong radio source (flux density ~22.5 Jy (Jy, jansky = 10^{-26} W m^{-2} Hz^{-1}) at 8495 MHz and 7.5 Jy at 2380 MHz [*Berge and Gulkis*, 1976]) and contributed notice-
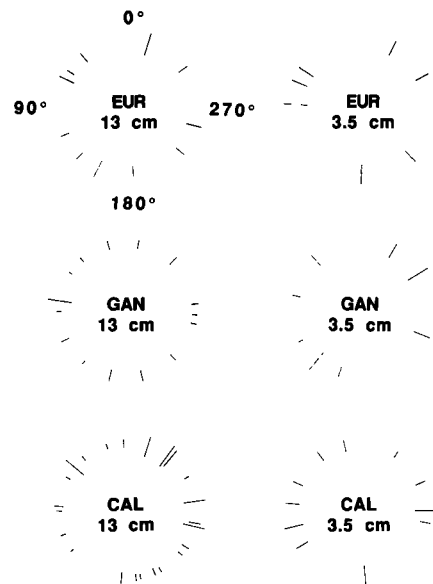

Fig. 1. Rotation/orbital phases ϕ of observations, as listed in Tables 4, 5, 6, and 7. ϕ also equals the west longitude of the subradar point. In each plot, the lengths of the line segments equal the rms receiver noise (Δx; see section 2) times a plotting scale factor. Each of the six plots uses a different scale factor.
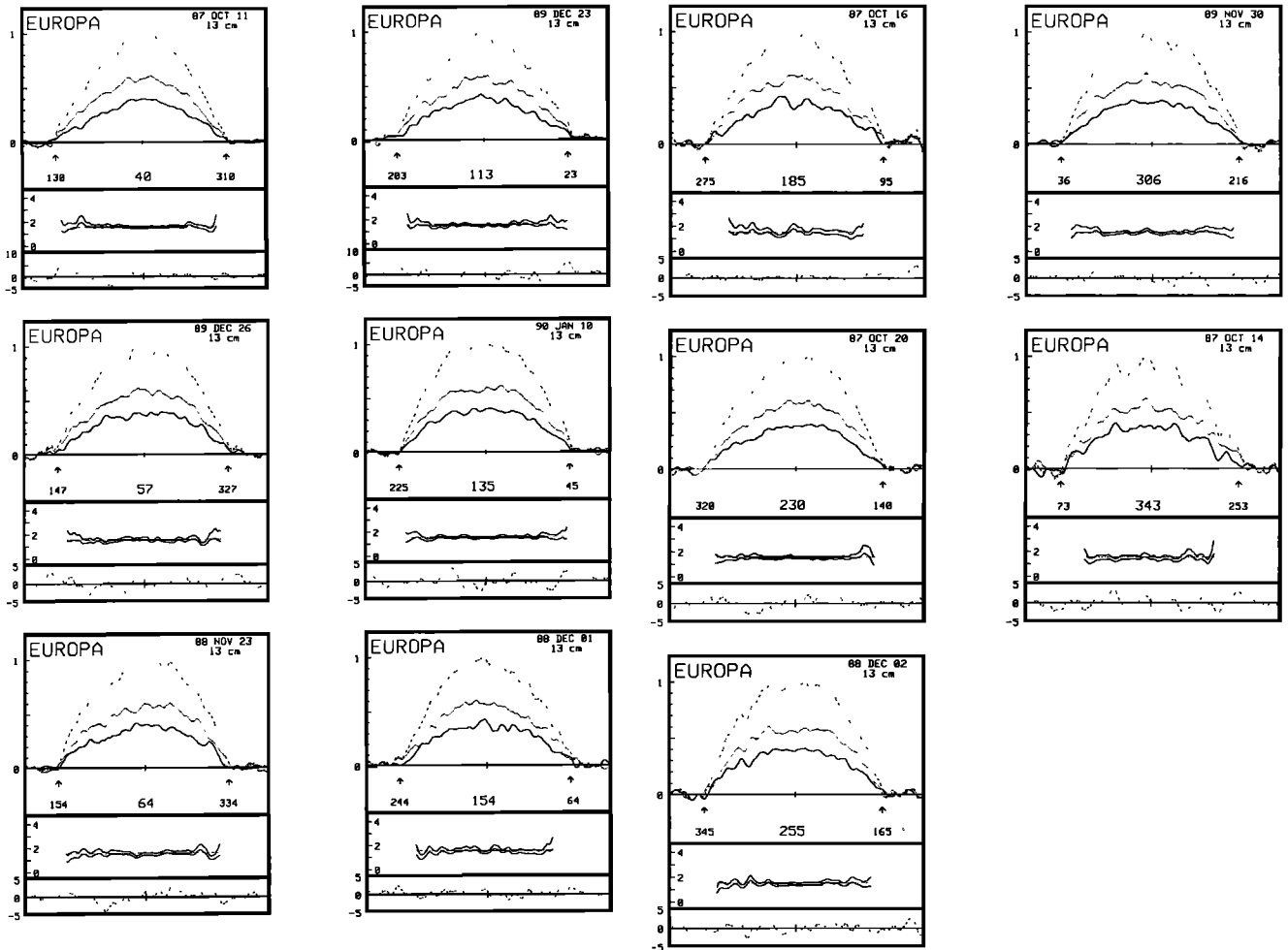
Fig. 2. Selected Arecibo 13-cm echo spectra, smoothed to a frequency resolution equal to 5% of the limb-to-limb bandwidth (Table 3). Each block has three panels that show results for echoes obtained on a single date (Table 4). In the top panel of each block, the OC, SC, and total power (T = OC + SC) spectra are plotted as solid, dotted, and dashed curves, respectively, normalized to the T spectrum's maximum. A vertical bar in the middle of the abscissa locates the frequency corresponding to echoes from the subradar point or, equivalently, to hypothetical echoes from the target's center of mass. The length of that bar represents ± 1 standard deviation of the single-channel receiver noise. The number under the noise bar is the rotation phase ϕ, i.e., the west longitude of the subradar point in degrees. Vertical arrows locate frequencies of echoes from the target's approaching (left) and receding (right) limbs and are labeled with longitudes plus and minus 90° from ϕ. In the middle panel of each block, two solid curves define the upper and lower limits of the standard error interval estimated for the circular polarization ratio μ_c = SC/OC according to the appendix. These curves cover the band within which the SC and OC power levels exceed five standard deviations of the noise. The dotted horizontal curve indicates the mean 13-cm value of μ_c for the target (Table 8). In the bottom panel of each block, we plot the residuals from the fit of a homogeneous spectral model to the total power spectrum. The ordinate has units of standard deviations and a noise bar is shown as in the top panel. Linear scales are used throughout.

ably to T_s for observations of targets less than about 5 arc min from the planet. For Goldstone observations, Jupiter's contribution was calculated from a model based on measurements, made on several dates during each opposition, of T_s as a function of the antenna's offset from Jupiter. For Arecibo, the data acquisition computer program managed the injection of a calibration noise pulse of known temperature into the receiver for 40 s once every 10 min, permitting direct estimation of the system temperature.

A "frequency-hopping" method was used to ensure accurate removal of the receiver's background noise baseline. The idea here was to use a receiving passband much wider than the echo bandwidth and to switch the transmitter frequency through N preset values in a manner that placed the echo at N different positions within that passband. At any given moment during a run's receive period, echo would be returning at only one of those N positions. Therefore at any given moment we were accumulating echo plus background at one of the N positions and a reliable sample of the background at the other N - 1 positions.

For all Arecibo observations, the transmitter was cycled among N = 4 different frequencies 2200 Hz apart and centered on 2380 MHz, dwelling a time τ_d = 10 s at each. For all Goldstone observations, the transmitter was switched back and forth between N = 2 frequencies 5000 Hz apart and centered on 8495 MHz, dwelling a time τ_d = 30 s at each. Then, in post-real time for Goldstone and in either real time or post-real time for Arecibo, echo spectra were accumulated over intervals of duration τ_d, the start of each interval being delayed by the roundtrip flight time to maintain synchronism with the transmitted sequence.
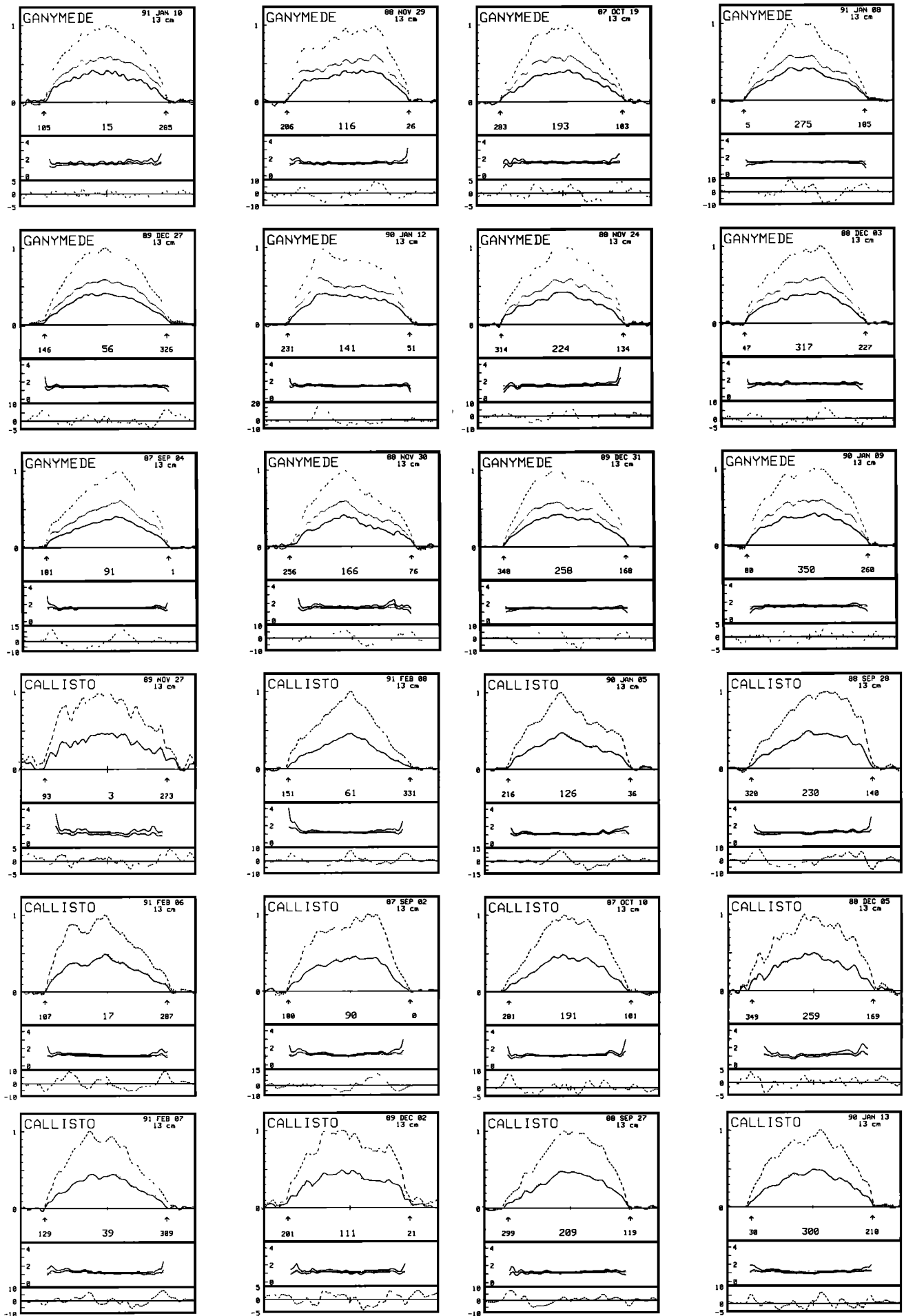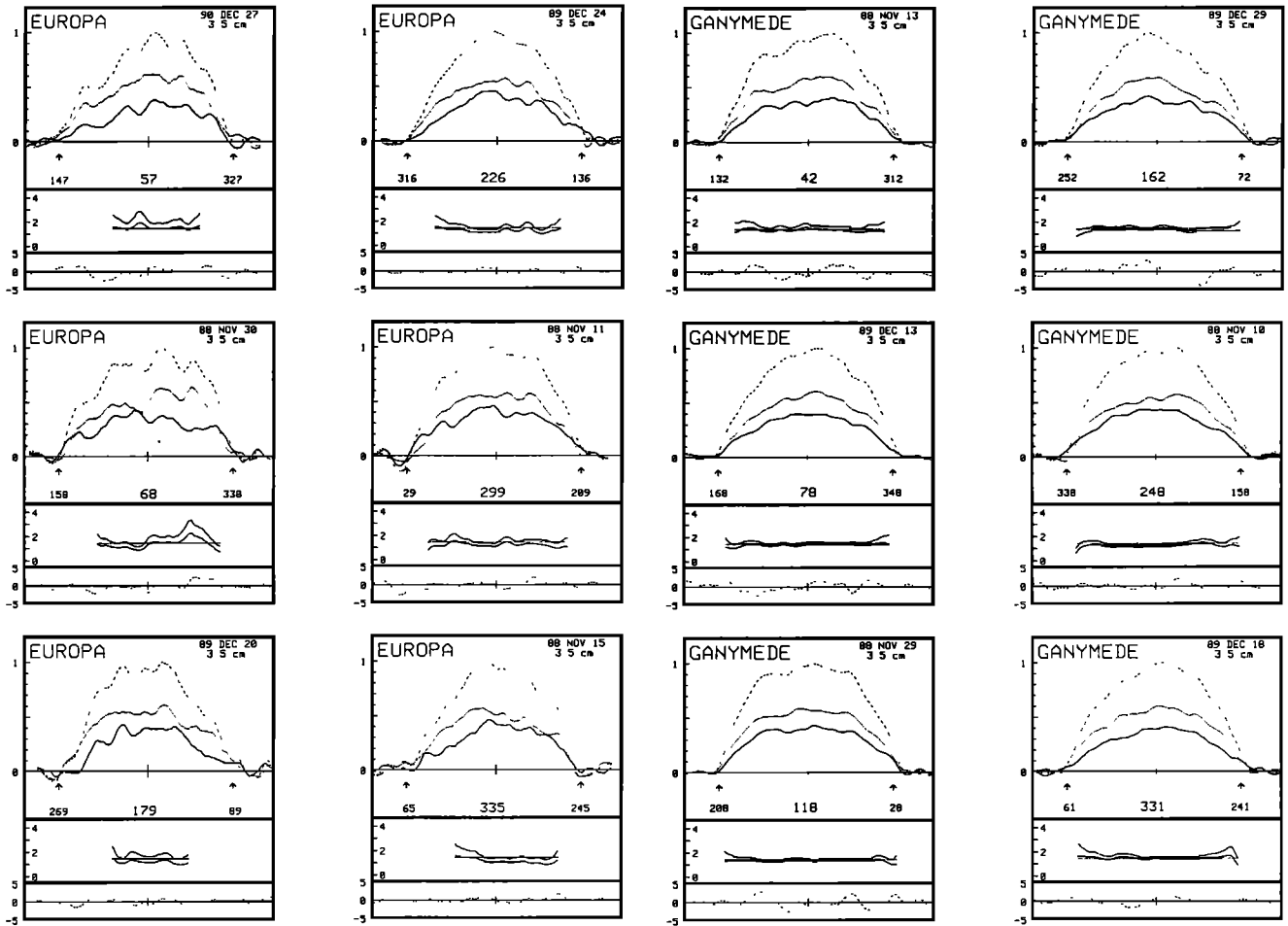
Fig. 2. (continued)

Fig. 3. Selected Goldstone 3.5-cm echo spectra, smoothed to a frequency resolution equal to 10% of the limb-to-limb bandwidth (Table 3). Each block has three panels that show results for echoes obtained on a single date (Table 5). See Figure 2 caption.

Let τ_{run} denote the total data accumulation time for a run, typically ~1.2 hours. We reduced the data in blocks of duration $\tau = MN\tau_d < \tau_{run}$, with M equal to 6 for Arecibo and 10 for Goldstone, as follows. For each transmitter frequency f_j, we summed the M spectra corresponding to that frequency. Thus we accumulated N raw spectra $r_1, r_2,..., r_N$, where boldface denotes a one-dimensional array. The background for r_j is

$$b_j = \sum_{i \neq j} r_i/(N - 1) \qquad (1)$$

The background-free spectra in units of the mean noise power are

$$s_j = (r_j - b_j)/b_j \qquad (2)$$

Since the block's total integration time τ was divided equally over N transmitter frequencies, the fractional rms noise in each r_j is

$$\Delta r = (B\tau/N)^{-1/2} \qquad (3)$$

where B is the spectral resolution. The fractional rms noise in each b_j is

$$\Delta b = (B\tau/N)^{-1/2}(N - 1)^{-1/2} \qquad (4)$$

Thus the rms noise in each s_j is easily calculated:

$$(\Delta s)^2 = (\Delta r)^2 + (\Delta b)^2 \qquad (5)$$

$$(\Delta s)^2 = N/B\tau + N/B\tau(N - 1) \qquad (6)$$

$$\Delta s = N/[B\tau(N - 1)]^{1/2} \qquad (7)$$

The final step is to add the N properly shifted s_j, resulting in a further $1/N^{1/2}$ reduction in the rms noise. The resultant power spectrum, in units of the rms noise fluctuation, is

$$x = \sum_{j=1}^{N} s_j/\Delta x \qquad (8)$$

where

$$\Delta x = \Delta s/N^{1/2} = [N/(N - 1)B\tau]^{1/2} \qquad (9)$$

For a given $B\tau$ product, the noise is proportional to $[N/(N-1)]^{1/2}$, which equals 1.41 and 1.16 for N equal to 2 and 4,
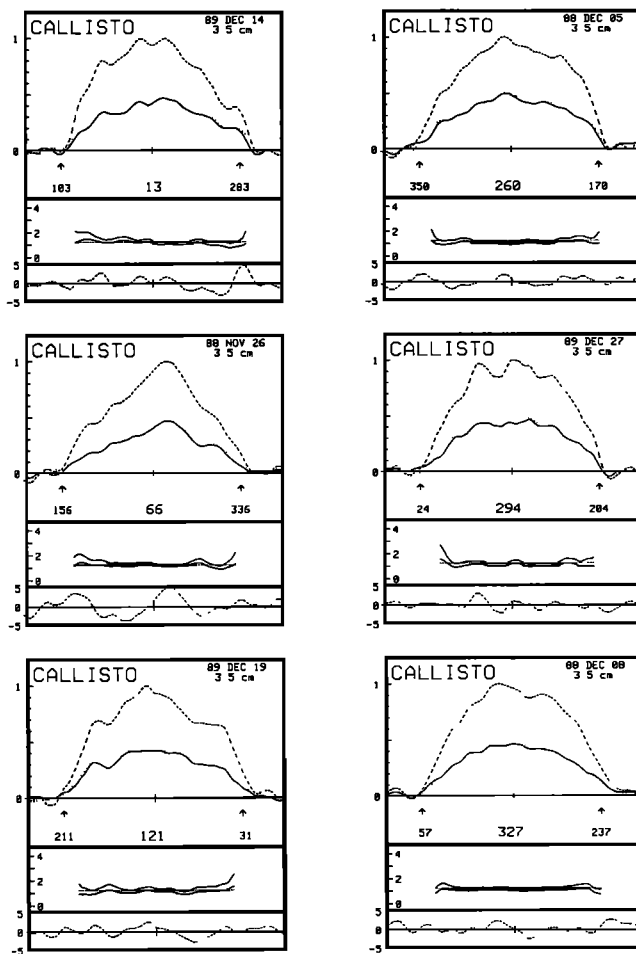
Fig. 3. (continued)

respectively. Hence the use of four transmitter frequencies at Arecibo gained a factor of about 1.2 in signal-to-noise ratio over that obtainable with two frequencies. At Goldstone, values of N larger than 2 were precluded by the combination of sampling-rate limitations and the fact that the satellites' echo bandwidths at Goldstone's transmitter frequency are 3.6 times larger than at Arecibo's (Table 3).

For Arecibo observations, the sampling rate was 11 kHz and a 2048-point fast Fourier transform (FFT) was used in the spectral analysis, yielding a frequency resolution of 5.4 Hz. For Goldstone observations, the sampling rate was 10 kHz and a 512-point FFT was used, yielding a frequency resolution of 20 Hz. Thus for all our observations, the resolution of the reduced spectra was between 0.5% and 2% of the echo's bandwidth.

In carrying out the data reduction described above, we used block integration times τ equal to 4 min for Arecibo and 10 min for Goldstone. Thus, for example, an hour of data would be reduced to 15 OC/SC pairs of spectra for Arecibo or six pairs for Goldstone. In our working data set, each spectrum is in units of the rms receiver noise fluctuation Δx and is tagged with the numerical value of Δx (square kilometers) of radar cross section per frequency resolution cell. That value varied during the observation because it is a function of the transmit and receive antenna gain and the system temperature, which depend on zenith angle. Our data reduction protocol made it easy to form correctly weighted, properly calibrated, single-run or multirun sums of single-block spectra. All analyses presented in this paper used single-date spectra, that is, weighted sums of spectra obtained for a particular target from observations on a single date.

Tables 4 and 5 list the dates, times, and mean rotation phases ϕ of our observations in chronological order for Europa, Ganymede, and Callisto. The intrinsic rotation phase resolution of the single-date spectra ranges from about 1° for single runs on Callisto to about 16° for two consecutive runs on

TABLE 6. Results of Analyses of Single-Date Arecibo Spectra

Target	UTC Date	Phase (ϕ)	SNR	RRC	n	SC/OC Ratio μ_c	$\hat{\sigma}_{OC}$	$\hat{\sigma}_{SC}$	$\hat{\sigma}_T$
EUR	Oct. 11, 1987	40°	150	1.1	2.1	1.58 ± 0.02	1.045	1.65	2.70
EUR	Dec. 26, 1989	57°	110	1.1	1.6	1.51 ± 0.03	[0.661	1.00	1.66]
EUR	Nov. 23, 1988	64°	100	1.0	1.6	1.53 ± 0.03	1.037	1.59	2.62
EUR	Dec. 23, 1989	113°	130	1.1	1.7	1.52 ± 0.03			
EUR	Jan. 10, 1990	135°	150	1.1	1.7	1.52 ± 0.02	0.925	1.41	2.33
EUR	Dec. 1, 1988	154°	90	1.1	1.9	1.51 ± 0.04	1.061	1.61	2.67
EUR	Oct. 16, 1987	185°	77	1.0	2.1	1.57 ± 0.04	1.165	1.83	3.00
EUR	Oct. 20, 1987	230°	130	1.1	1.9	1.52 ± 0.03	0.881	1.34	2.22
EUR	Dec. 2, 1988	255°	100	1.0	1.7	1.48 ± 0.03	1.043	1.55	2.59
EUR	Nov. 30, 1989	306°	120	1.0	1.7	1.53 ± 0.03			
EUR	Oct. 14, 1987	343°	76	1.1	1.8	1.50 ± 0.04	1.085	1.63	2.71
GAN	Jan. 10, 1991	15°	120	1.0	1.4	1.50 ± 0.03	0.444	0.667	1.11
GAN	Sept. 3, 1987	41°	220	1.1	1.6	1.50 ± 0.01	0.494	0.740	1.24
GAN	Dec. 27, 1989	56°	260	1.3	1.5	1.43 ± 0.01	0.478	0.683	1.16
GAN	June 24, 1987	82°	41	1.0	1.8	1.50 ± 0.04	0.598	0.897	1.50
GAN	Sept. 4, 1987	91°	270	1.7	1.7	1.52 ± 0.01	0.574	0.873	1.45
GAN	Nov. 29, 1988	116°	170	1.3	1.1	1.45 ± 0.02	0.600	0.871	1.47
GAN	Jan. 12, 1990	141°	270	1.7	1.1	1.40 ± 0.01	0.519	0.726	1.25
GAN	Nov. 30, 1988	166°	130	1.3	1.7	1.52 ± 0.03	0.558	0.848	1.41
GAN	Oct. 19, 1987	193°	150	1.1	1.8	1.52 ± 0.02			
GAN	Nov. 24, 1988	224°	170	1.2	1.4	1.47 ± 0.02	0.604	0.888	1.49
GAN	Dec. 31, 1989	258°	290	1.4	1.4	1.39 ± 0.01	0.610	0.849	1.46
GAN	Dec. 24, 1989	266°	280	1.6	1.4	1.35 ± 0.01			
GAN	Jan. 8, 1991	275°	250	1.5	1.7	1.37 ± 0.01	0.639	0.876	1.52
GAN	Dec. 3, 1988	317°	180	1.2	1.7	1.48 ± 0.02	0.633	0.937	1.57
GAN	Jan. 9, 1990	350°	180	1.1	1.3	1.47 ± 0.02	0.595	0.875	1.47

TABLE 6. (continued)

Target	UTC Date	Phase (φ)	SNR	RRC	n	SC/OC Ratio μc	$\hat{\sigma}_{OC}$	$\hat{\sigma}_{SC}$	$\hat{\sigma}_{T}$
CAL	Nov. 27, 1989	3°	59	1.1	0.9	1.18 ± 0.04			
CAL	Feb. 6, 1991	17°	140	1.5	1.5	1.18 ± 0.02	0.298	0.352	0.650
CAL	Feb. 7, 1991	39°	150	1.3	2.0	1.23 ± 0.02	0.297	0.366	0.664
CAL	June 25, 1987	50°	42	1.0	2.7	1.20 ± 0.06	0.328	0.393	0.721
CAL	Feb. 8, 1991	61°	150	1.3	2.4	1.24 ± 0.02	0.293	0.364	0.657
CAL	Nov. 27, 1988	86°	110	1.2	1.7	1.20 ± 0.02	0.329	0.394	0.723
CAL	Sept. 2, 1987	90°	150	1.4	1.6	1.24 ± 0.02			
CAL	Oct. 22, 1987	91°	210	1.6	1.5				0.792
CAL	Dec. 2, 1989	111°	90	1.1	1.0	1.15 ± 0.03			
CAL	Jan. 5, 1990	126°	180	1.6	1.4	1.15 ± 0.01	0.286	0.330	0.616
CAL	Jan. 11, 1991	175°	66	1.0	1.9	1.22 ± 0.04	0.272	0.332	0.604
CAL	Sept. 26, 1988	187°	120	1.1	1.9	1.23 ± 0.02	0.302	0.371	0.673
CAL	Oct. 10, 1987	191°	190	1.2	2.0	1.19 ± 0.01	0.346	0.411	0.757
CAL	Sept. 10, 1988	203°	72	1.0	2.0	1.17 ± 0.03	[0.182	0.213	0.394]
CAL	Sept. 27, 1988	209°	160	1.2	2.1	1.16 ± 0.01	0.307	0.356	0.663
CAL	Sept. 28, 1988	230°	160	1.5	1.6	1.17 ± 0.01	0.307	0.360	0.668
CAL	Dec. 4, 1988	238°	110	1.2	1.5	1.12 ± 0.02	0.350	0.392	0.742
CAL	Dec. 2, 1987	256°	45	1.0	1.1	1.14 ± 0.05	0.364	0.415	0.779
CAL	Dec. 5, 1988	259°	74	1.1	1.1	1.12 ± 0.03	0.323	0.361	0.684
CAL	Dec. 3, 1987	278°	47	1.0	1.1	1.14 ± 0.05	0.364	0.415	0.779
CAL	Jan. 13, 1990	300°	160	1.2	1.2	1.10 ± 0.01	0.293	0.323	0.616
CAL	Dec. 5, 1987	321°	47	1.0	1.3	1.19 ± 0.05	0.340	0.404	0.744
CAL	June 21, 1987	324°	36	1.0	0.9	1.10 ± 0.06	0.329	0.362	0.697
CAL	Dec. 6, 1987	343°	44	1.0	1.1	1.21 ± 0.06	0.321	0.388	0.709

We list estimates of the ratio $\mu_c = \sigma_{SC}/\sigma_{OC}$ and the radar albedos $\hat{\sigma}_{OC}$ $\hat{\sigma}_{SC}$ and $\hat{\sigma}_{T}$. As discussed in the text, SNR is the signal-to-noise ratio for the total power spectrum and RRC is root-reduced chi-square for the least squares estimation of Doppler frequency f_0 (see text and Table 4) and scattering law exponent n. The standard error in the estimate of n never exceeds 0.1. Absolute uncertainties in albedo estimates are probably between 20% and 50%, and relative (run-to-run and date-to-date) uncertainties are probably about 15%. Uncertainties quoted for the SC/OC ratio μ_c are standard errors due to receiver noise fluctuations (the appendix). On seven dates, instrumental/calibration difficulties precluded reliable estimation of single-polarization albedos but did not undermine estimation of the SC/OC ratio. For two dates, the albedo (in brackets) is much lower than values at nearby phases; these outliers probably resulted from antenna pointing errors and have been excluded from all analyses in this paper. For the October 22, 1987, observations of Callisto, the telescope was configured for linearly polarized transmission and reception; the only results of those observations used in this paper are from the total power spectrum.

TABLE 7. Results of Analyses of Single-Date Goldstone Spectra

Target	UTC Date	Phase (φ)	SNR	RRC	n	SC/OC Ratio μc	$\hat{\sigma}_{OC}$	$\hat{\sigma}_{SC}$	$\hat{\sigma}_{T}$
EUR	Dec. 27, 1990	57°	34	1.0	1.8 ± 0.2	1.85 ± 0.12	0.738	1.37	2.10
EUR	Nov. 30, 1988	68°	38	1.1	1.3 ± 0.2	1.47 ± 0.07	1.077	1.58	2.66
EUR	Nov. 16, 1988	87°	20	1.3	1.2 ± 0.3	1.77 ± 0.16	1.04	1.85	2.89
EUR	Dec. 20, 1989	179°	27	0.9	2.0 ± 0.3	1.73 ± 0.13	0.803	1.39	2.19
EUR	Dec. 24, 1989	226°	45	0.9	1.8 ± 0.2	1.39 ± 0.06	0.963	1.34	2.30
EUR	Nov. 11, 1988	299°	46	1.0	1.7 ± 0.2	1.30 ± 0.05	0.965	1.25	2.22
EUR	Nov. 15, 1988	335°	34	1.1	2.3 ± 0.3	1.38 ± 0.08	0.755	1.04	1.80
GAN	Nov. 13, 1988	42°	58	1.1	1.5 ± 0.1	1.52 ± 0.05	0.451	0.686	1.14
GAN	Dec. 13, 1989	78°	97	1.1	1.4 ± 0.1	1.46 ± 0.03	0.639	0.934	1.57
GAN	Nov. 29, 1988	118°	110	1.0	1.1 ± 0.1	1.41 ± 0.03	0.681	0.960	1.64
GAN	Nov. 22, 1988	140°	60	1.0	1.2 ± 0.1	1.20 ± 0.04	0.733	0.880	1.61
GAN	Dec. 29, 1989	162°	82	1.1	1.4 ± 0.1	1.42 ± 0.04	0.621	0.883	1.51
GAN	Nov. 10, 1988	248°	81	1.0	1.3 ± 0.1	1.30 ± 0.03	0.791	1.025	1.82
GAN	Dec. 18, 1990	301°	33	1.0	1.7 ± 0.2	1.45 ± 0.08	[0.379	0.550	0.93]
GAN	Dec. 18, 1989	331°	80	1.1	1.4 ± 0.1	1.52 ± 0.04	0.618	0.940	1.56
CAL	Dec. 14, 1989	13°	62	1.1	1.4 ± 0.1	1.28 ± 0.04	0.356	0.456	0.812
CAL	Dec. 15, 1989	35°	58	1.1	1.7 ± 0.1	1.23 ± 0.04	0.316	0.388	0.704
CAL	Nov. 26, 1988	66°	66	1.2	1.8 ± 0.1	1.28 ± 0.04	0.362	0.464	0.826
CAL	Nov. 10, 1988	84°	46	1.1	1.3 ± 0.1	1.39 ± 0.06	0.308	0.428	0.735
CAL	Dec. 22, 1990	104°	34	1.1	1.0 ± 0.2	1.27 ± 0.07	0.310	0.393	0.703
CAL	Dec. 19, 1989	121°	48	1.0	1.1 ± 0.1	1.25 ± 0.05	0.302	0.377	0.679

TABLE 7. (continued)

Target	UTC Date	Phase (ϕ)	SNR	RRC	n	SC/OC Ratio μ_C	$\hat{\sigma}_{OC}$	$\hat{\sigma}_{SC}$	$\hat{\sigma}_T$
CAL	Dec. 22, 1989	185°	30	1.1	1.7 ± 0.3	1.20 ± 0.08	0.340	0.407	0.747
CAL	Dec. 5, 1988	260°	63	1.0	1.1 ± 0.1	1.14 ± 0.04	0.341	0.388	0.729
CAL	Dec. 13, 1990	270°	18	1.0	1.4 ± 0.4	1.32 ± 0.14	[0.171	0.226	0.40]
CAL	Dec. 27, 1989	294°	54	1.1	1.5 ± 0.1	1.17 ± 0.04	0.298	0.349	0.647
CAL	Dec. 8, 1988	327°	80	1.0	1.3 ± 0.1	1.16 ± 0.03	0.306	0.354	0.659

We list estimates of the ratio $\mu_C = \sigma_{SC}/\sigma_{OC}$ and the radar albedos $\hat{\sigma}_{OC}$, $\hat{\sigma}_{SC}$, and $\hat{\sigma}_T$. As discussed in the text, SNR is the signal-to-noise ratio for the total power spectrum and RRC is root-reduced chi-square for the least squares estimation of Doppler frequency f_0 (see text and Table 5) and scattering law exponent n. Absolute uncertainties in albedo estimates are probably between 20% and 50%, and relative (run-to-run and date-to-date) uncertainties are probably about 15%. Uncertainties quoted for the SC/OC ratio μ_C are standard errors due to receiver noise fluctuations (the appendix). For two dates, the albedos (in brackets) are much lower than values measured at nearby phases; these outliers probably resulted from antenna pointing errors and have been excluded from all analyses in this paper.
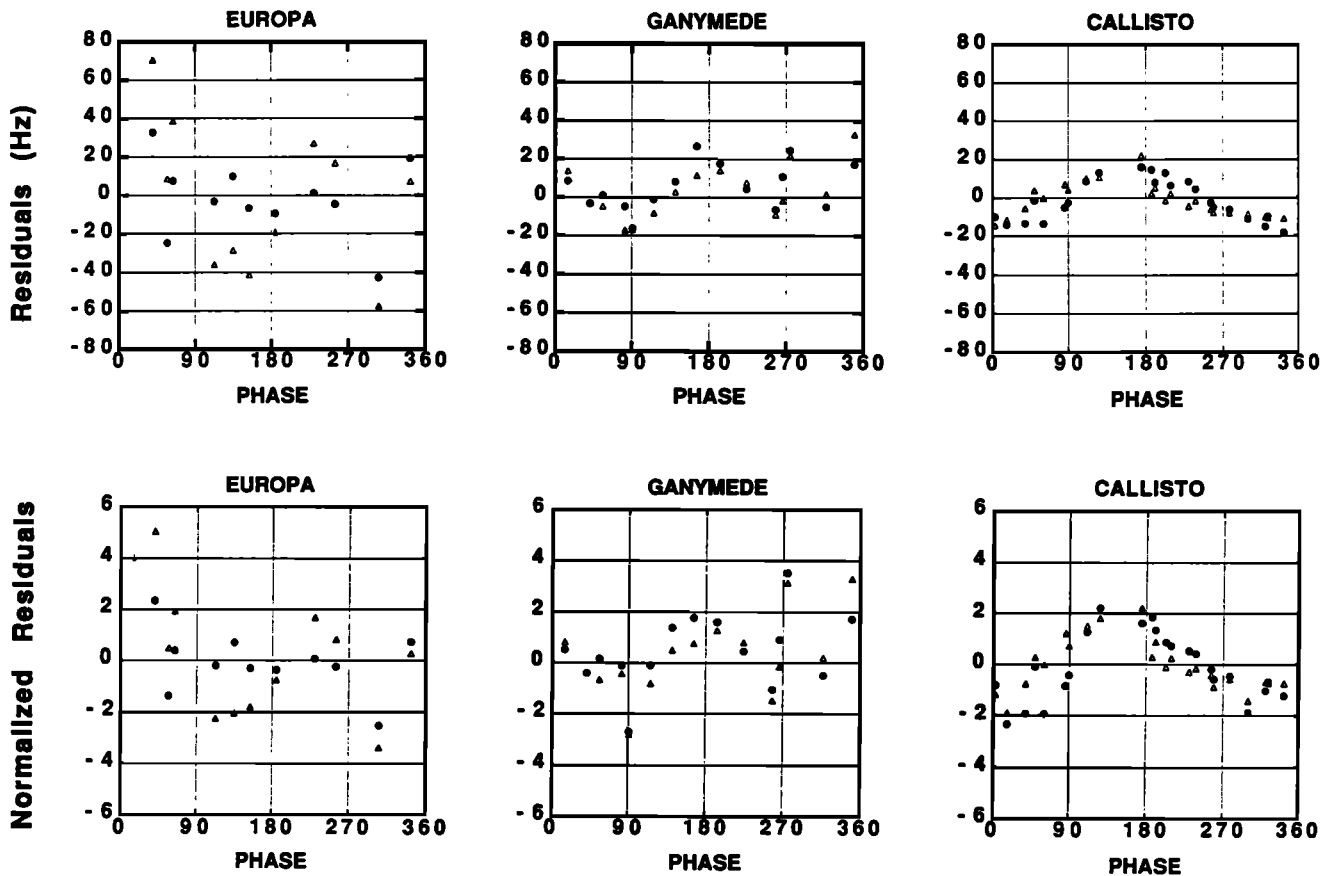
Fig. 4. Differences between our Arecibo estimates of f_{COM} and predictions based upon the JPL planetary ephemeris DE200 [Standish, 1990] combined with an updated version (E-3) of the satellite ephemeris E-2 [Lieske, 1980]. Residuals calculated using either DE202 (an updated version of DE200) or the CfA planetary ephemeris PEP740 are within 1 Hz of those plotted here. The solid circles correspond to Doppler estimates in Table 4. The triangles correspond to frequencies estimated as part of the Doppler mapping inversions discussed in section 5. The top row shows the residuals in Hz. In the bottom row, the residuals have been normalized to the Doppler estimation errors in Table 4.

Europa. Because of the satellites' spin orbit synchronism, the geocentric rotation phase and orbital phase are the same as the subradar point's longitude, when measured west from the Jupiter-facing meridian. Figure 1 shows our data's rotation phase coverage of each target and also indicates the relative noise level in the (single-date) spectra.

3. ANALYSIS OF ECHO SPECTRA

Figures 2 and 3 show selected single-date spectra smoothed to 5% of the limb-to-limb bandwidth for Arecibo and 10% for Goldstone. Estimates of the OC and SC radar cross sections σ_{OC} and σ_{SC} were obtained by integrating over the spectra. Here

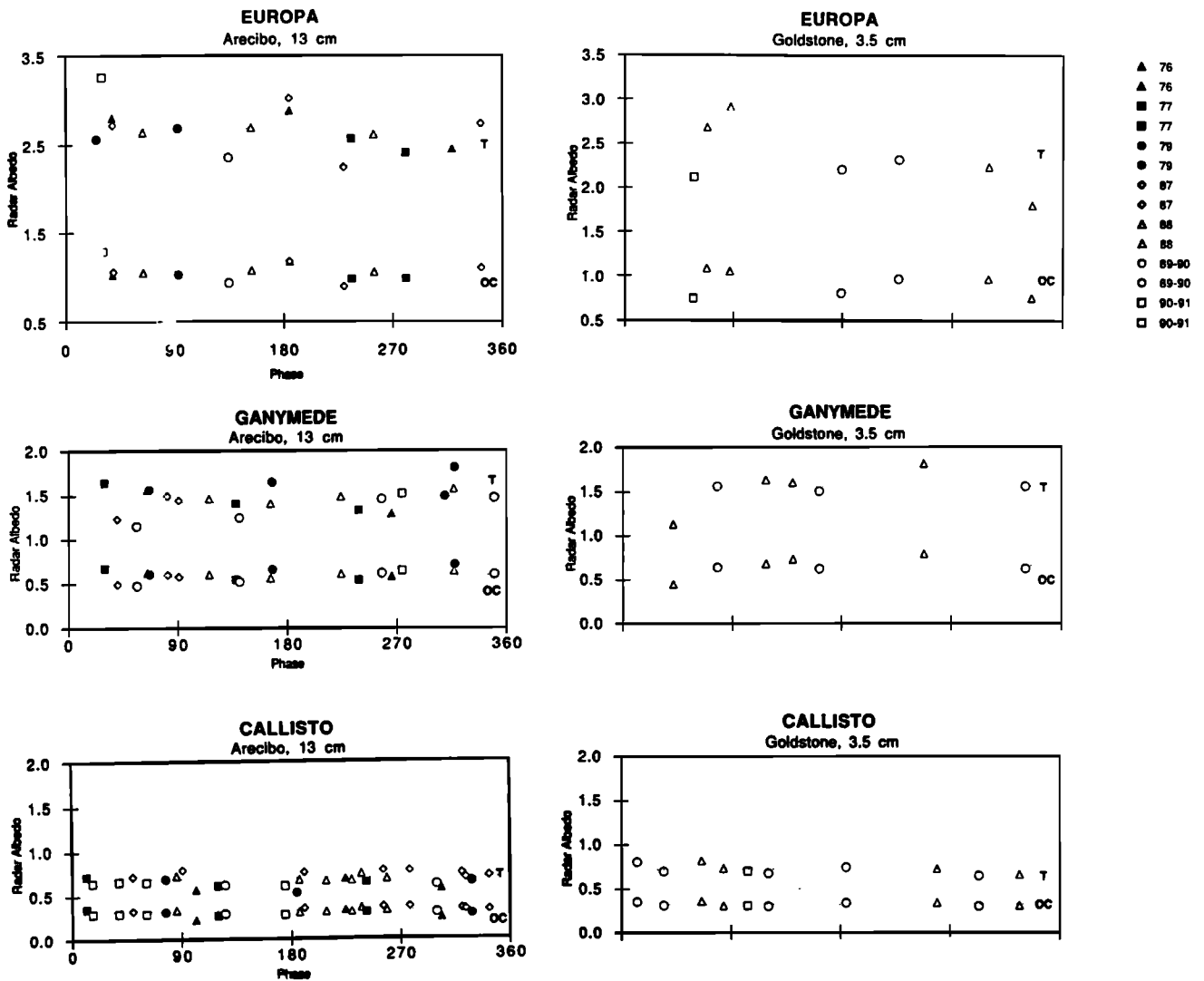# Radar Albedos ($\hat{\sigma}_T$ and $\hat{\sigma}_{OC}$)

Fig. 5. Estimates of $\hat{\sigma}_T$, $\hat{\sigma}_{OC}$, and μ_C versus ϕ, as listed in Tables 6 and 7. Dotted horizontal lines show mean values from Table 8. The Arecibo 13-cm plots include results of 1976-1979 observations reported by Campbell et al. [1978] and Ostro et al. [1980].

we report normalized radar cross sections, or "radar albedos," defined by $\hat{\sigma} = 4\sigma/\pi D^2$, with D the satellite diameter (Table 3). Tables 6 and 7 list estimates of the OC and SC radar albedos, the total power radar albedo $\hat{\sigma}_T = \hat{\sigma}_{OC} + \hat{\sigma}_{SC}$, and the circular polarization ratio $\mu_C = \sigma_{SC}/\sigma_{OC}$.

Uncertainties in radar albedo estimates are dominated by systematic uncertainties in radar system sensitivity, i.e., in pointing, gain calibration, system temperature calibration, Jupiter's contribution to system temperature, and transmitter power calibration. We believe absolute uncertainties in albedo estimates to be between 20% and 50%, and relative (run-to-run and date-to-date) uncertainties to be about 15%. Uncertainties quoted for μ_C are standard errors due to receiver noise fluctuations (see the appendix). Systematic sources of error in estimates of the SC/OC ratio can arise from cross-coupling between the two receiver channels or from errors in calibrating the two channels' relative system temperatures; these errors are probably on the order of several percent for the observations

reported here. Tables 6 and 7 also list the signal-to-noise ratio, SNR, of each total power spectrum when optimally filtered, that is, when smoothed to a resolution equal to the spectrum's equivalent bandwidth B_{EQ}. By definition [Tiuri, 1964], $B_{EQ}/\Delta f = (\Sigma y_i)^2/\Sigma y_i^2$, where the unsmoothed spectral estimates y_i have frequency resolution Δf. For most of our spectra, the ratio B_{EQ}/B is between 0.8 and 0.9, with B the limb-to-limb bandwidth (Table 3).

We used weighted-least squares to fit to each total power spectrum a parameterized model of the form $S(f) \sim [1 - (f - f_0)^2/(B/2)^2]^{n/2}$, where $f_0 = f_{COM}(t) - f_{BPH}(t)$ as noted above. This function describes the spectral shape for echoes from a spherical target with a uniform scattering law, $\sigma_0(\theta) = d\sigma/dA \sim \cos^n\theta$, where dA is an element of surface area and θ is the angle of incidence measured from the element's outward normal. Tables 6 and 7 list our estimates of the scattering law exponent n and the value of root reduced chi-square
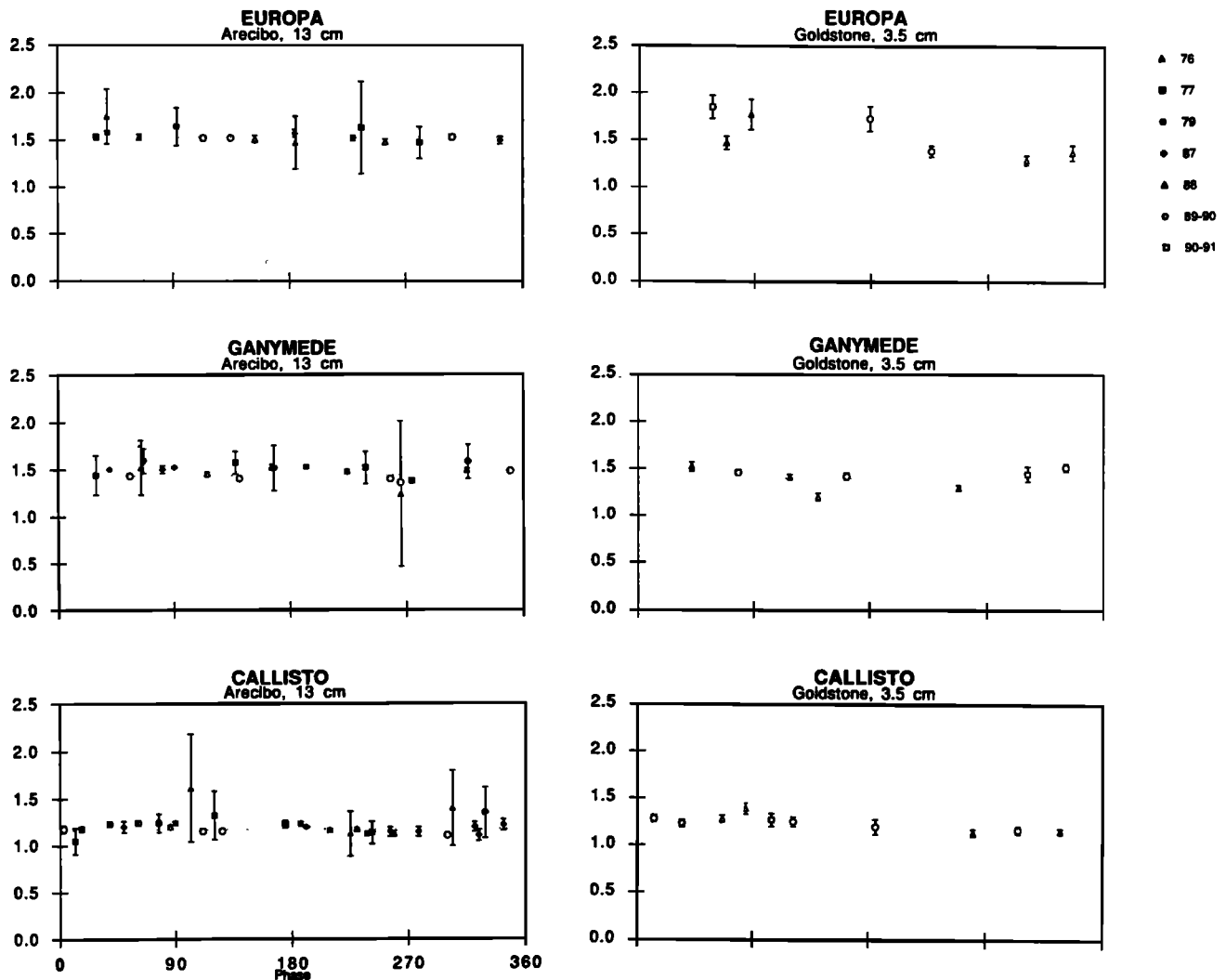
Circular Polarization Ratio (μ_C = SC/OC)

Fig. 5. (continued)

(RRC, the root-sum-square of the postfit residuals) for each estimation. The S(f) model is symmetric but many of our spectra are not, so the estimates of n and f_0 might be biased.

To explore biases in least squares estimates of f_0, we also estimated that quantity in a different way, as follows. Given any candidate value of f_0, we flipped the spectrum about that frequency, added the flipped and unflipped spectra together to make a spectrum that was symmetric about f_0, and measured that spectrum's bandwidth $B'(f_0)$ between the two zero crossings closest to f_0. We expect B' to be minimized (and close to the limb-to-limb bandwidth B in Table 3) at the "true" value of f_0. The bandwidth minimization estimates were noticeably different from the least squares estimates for about half of the Arecibo Callisto spectra and about one third of the Arecibo Ganymede spectra; for these we adopted a subjectively weighted average of the two estimates. For all Goldstone spectra and Arecibo Europa spectra, we adopted the least squares values.

We added the adopted values of f_0 to the ephemeris predictions at the weighted-mean receive times t_0 listed in Tables 4 and 5, which list the resultant estimates of $f_{COM}(t_0)$. The uncertainty assigned to each Doppler estimate is greater than or equal to (1) Δf, (2) 2B/SNR, (3) 5 times the standard error in the least squares value, and (4) the difference between the values estimated by least squares and bandwidth minimization.

Figure 4 plots the differences between our Arecibo estimates of f_{COM} and predictions based upon the planetary ephemeris DE200 [Standish, 1990] combined with an updated version (E-3) of the satellite ephemeris E-2 [Lieske, 1980]. The most significant result of the measurements is the sinusoidal signature evident in the Callisto residuals. Our analysis of those residuals indicates that Callisto is lagging its ephemeris by 200 ± 50 km.

4. DISC-INTEGRATED RESULTS

Figure 5 plots our single-date estimates of $\hat{\sigma}_{OC}$, $\hat{\sigma}_T$, and μ_C versus ϕ along with estimates from 1976-1979 Arecibo observations [Campbell et al., 1978; Ostro et al., 1980]. Table 8 and Figure 6 show average values and rms dispersions of our values for $\hat{\sigma}_{OC}$, $\hat{\sigma}_{SC}$, $\hat{\sigma}_T$, μ_C, and n. Together, these results permit fairly definitive statements about the degree to

TABLE 8. Mean Radar Properties of Europa, Ganymede, and Callisto

		Arecibo 13-cm	Goldstone 3.5-cm
		SC/OC Ratio μ_c	
Europa		1.53 ± 0.03	1.43 ± 0.24
Ganymede		1.43 ± 0.06	1.40 ± 0.10
Callisto		1.17 ± 0.04	1.22 ± 0.08
		Radar Albedos	
Europa	OC	1.03 ± 0.08	0.91 ± 0.13
	SC	1.58 ± 0.14	1.40 ± 0.23
	T	2.60 ± 0.22	2.31 ± 0.36
Ganymede	OC	0.57 ± 0.06	0.65 ± 0.10
	SC	0.82 ± 0.09	0.90 ± 0.10
	T	1.39 ± 0.14	1.55 ± 0.20
Callisto	OC	0.32 ± 0.03	0.32 ± 0.02
	SC	0.37 ± 0.03	0.40 ± 0.04
	T	0.69 ± 0.06	0.72 ± 0.06
		Total Power Scattering Law Exponent n	
Europa		1.8 ± 0.2	1.7 ± 0.4
Ganymede		1.5 ± 0.2	1.3 ± 0.2
Callisto		1.5 ± 0.5	1.4 ± 0.3

For μ_c and n we give the statistically weighted mean of the single-date values in Tables 6 and 7 and the rms dispersion of the single-date values about the weighted mean. For the radar albedos $\hat{\sigma}_{OC}$, $\hat{\sigma}_{SC}$, and $\hat{\sigma}_T$, we give the unweighted mean and rms dispersion of the single-date values. See Figure 6.

which the radar properties of the icy Galilean satellites depend on target, wavelength, time and rotation phase, as follows.

The 1976-1991 Arecibo results are consistent with each other and show very little dependence of disc-integrated properties on rotation phase. The fractional rms variation in estimates of the SC/OC ratio μ_c is only a few percent for each satellite. On the other hand, the fractional rms variation in the OC, SC, and T (total power) albedos is at the 10% level for each satellite. For Ganymede and Callisto, this variation is readily understandable, because albedo features are prominent on these objects. For Europa, some of the variance in the albedo estimates might be caused by errors in calibrating Jupiter's contribution to the system temperature.

The mean 13-cm radar albedos and circular polarization ratios from the 1987-1991 Arecibo observations (Table 8 and Figure 6) are consistent with, but much more precise and relatively more accurate than, corresponding values estimated from observations in the 1970s (Table 1). The radar reflectivities of Europa, Ganymede, and Callisto are approximately in the ratio 4:2:1. Europa's mean value of μ_c is roughly 7% larger than Ganymede's, which in turn is some 20% larger than Callisto's.

Within the uncertainties, the satellites' mean radar properties are nearly the same at 3.5 cm and 13 cm. Table 9 and Figure 7 show the ratio γ of the Arecibo 13-cm estimate to the Goldstone 3.5-cm estimate for each quantity in Table 8. Ganymede and Callisto have $\gamma(\mu_c)$ within about 10% of unity and $\gamma(\sigma_T)$ within about 20% of unity. Hence for these two satellites our Arecibo and Goldstone observations and the 1976-1979 Arecibo observations favor the hypothesis that μ_c and σ_T are almost the same at 3.5 and 13 cm. For Europa, μ_c and σ_T might be slightly larger at 13 cm.
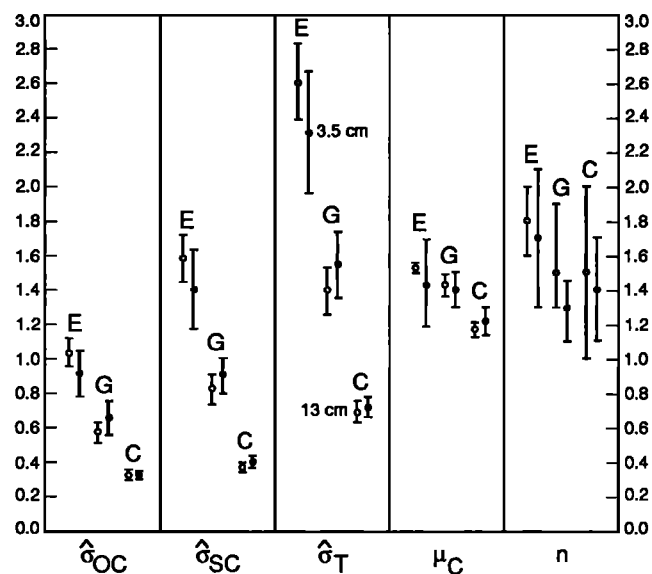

Fig. 6. Average values and rms dispersions of our values for $\hat{\sigma}_{OC}$, $\hat{\sigma}_{SC}$, $\hat{\sigma}_T$, μ_c, and n, as listed in Table 8.

TABLE 9. The Ratio γ of the Arecibo 13-cm Value to the Goldstone 3.5-cm Value for the Radar Properties in Table 8

		Lower Limit	Estimate	Upper Limit
		$\gamma(\mu_c)$		
Europa		0.92	1.07	1.29
Ganymede		0.94	1.02	1.11
Callisto		0.89	0.96	1.03
		$\gamma(Albedos)$		
Europa	OC	0.97	1.13	1.34
	SC	0.94	1.13	1.38
	T	0.95	1.13	1.36
Ganymede	OC	0.73	0.88	1.06
	SC	0.78	0.91	1.07
	T	0.76	0.90	1.06
Callisto	OC	0.89	1.00	1.12
	SC	0.81	0.92	1.05
	T	0.85	0.96	1.08
		$\gamma(n)$		
Europa		0.83	1.06	1.41
Ganymede		0.94	1.15	1.42
Callisto		0.68	1.07	1.56

Values were calculated according to the Appendix, with the uncertainties in Table 8 treated as standard errors. See Figure 7.

Our results suggest that previously reported estimates of Ganymede's μ_c and $\hat{\sigma}_T$ from Goldstone observations in the 1970s, as well as estimates of all three satellites' albedos from Arecibo observations in 1975, were afflicted by calibration errors. (See Table 1.)
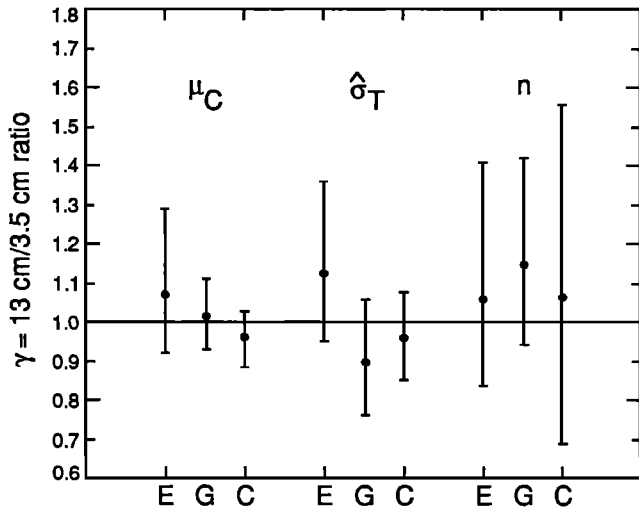
Fig. 7. Estimates of the ratio γ of the Arecibo 13-cm value to the Goldstone 3.5-cm value for the radar properties in Table 8. See Table 9.

Finally, we note that our 13-cm and 3.5-cm mean values for total power scattering law exponent agree with the previously reported 13-cm results. Estimates of n for Ganymede and Callisto are indistinguishable and smaller than Europa's. If the satellite surfaces were featureless, one could take these results to suggest that Europa is more limb-darkened or has brighter poles than the other two icy satellites. However, as discussed in section 5, the prominent postfit residuals in Figures 2 and 3 reveal the presence of albedo features, some of which might bias estimates of n from single-date spectra.

5. DISC-RESOLVED RESULTS

An echo spectrum can be thought of as a one-dimensional image, a brightness scan across the satellite's disc through a slit parallel to the apparent spin vector. Our spectra are plotted with positive frequencies on the left and negative frequencies on the right, so a hypothetical, bright point feature on a satellite's equator at west longitude ϕ would manifest itself as a spike on the left edge of a spectrum taken at rotation phase ϕ - 90°, that is, with the feature on the approaching limb. The spike would be in the center of a spectrum taken at phase ϕ and at the right edge of a spectrum at ϕ + 90°. In a spectrum taken at phase ϕ_0, a surface feature at latitude θ and longitude ϕ, with ϕ_0 ≤ ϕ ≤ ϕ_0 + 90°, would show up as a spectral feature a fraction $[(\cos \theta) \sin (\phi - \phi_0)]$ of the way from the spectrum's center to its left edge. In general, the spectral location of echoes from nonpolar surface features would migrate from left to right as the target rotates.

The middle panels in Figures 2 and 3 reveal a general lack of prominent μ_C features. For all the spectra shown the μ_C interval estimate remains within one interval width of the mean value estimated for the target at the pertinent wavelength (Table 8). However, Figure 5 shows that disc-integrated values of μ_C estimated for Callisto at both 13 cm and 3.5 cm are slightly higher than average within about 30° of rotation phase 70° and slightly lower than average within 30° of 270°. Hints of rather broadband μ_C features also can be seen in the top and middle panels of the Callisto plots in Figures 2 and 3. For Europa and Ganymede, visual inspection of the spectra does not reveal any μ_C features.

On the other hand, there are highly significant reflectivity

features evident in our 13-cm total power spectra. For the Goldstone spectra, which are weaker and are shown at a coarser resolution, highly significant residuals are lacking, although in many cases one can see correlation between Arecibo and Goldstone spectra at similar phases. The rest of this section focuses exclusively on the Arecibo spectra.

Albedo Features in the 13-cm Spectra

Ganymede spectra between phases 91° and 166° are dominated by a dark, broadband feature centered around ϕ = 135°. More modest, more narrowband, bright and dark features are evident in the spectra between 224° and 317°.

Albedo features on Callisto seem at least as abundant as on Ganymede. Note for example the bright feature in the middle of the 61° spectrum and just left of center in the 126° spectrum.

For Europa, the left edge of the 40° spectrum is slightly depressed, perhaps because of a low-reflectivity equatorial region on the approaching limb. There are hints of small depressions in subsequent spectra at progressively lower frequencies (more toward the right).

Reflectivity Maps From Inversion of the 13-cm Spectra

We wish to identify the locations of the radar features on the satellite surfaces and to assess the degree to which radar properties correlate with geologic terrains or spectrophotometric units. From visual inspection of our spectra and Voyager maps we can tentatively associate two prominent radar albedo features with major geologic features: the low-albedo Ganymede feature centered near 135° with Galileo Regio and the high-albedo Callisto feature centered near 60° with the Valhalla basin.

More useful constraints on the nature and extent of the albedo features are provided by "global" inversion of the echo spectra. *Hudson and Ostro* [1990] introduced an approach to making radar reflectivity maps of spherical planetary objects that uses echo spectra acquired as a function of rotation phase and at an arbitrary number of subradar latitudes. The target's albedo distribution is represented by a truncated spherical harmonic series and the Doppler frequency/rotation phase distribution of echo power is expressed as a linear, analytic function of the series coefficients. These equations contain a radar scattering law, of the form $\cos^n\theta$, that is assumed to be uniform and azimuthally isotropic. To estimate the coefficients for the albedo distribution from an observed phase-Doppler distribution (i.e., from a set of echo spectra taken at different rotation phases), the inversion is formulated as a least squares problem and solved directly using singular value decomposition. In our Doppler-mapping inversions, each spectrum's frequency offset from the ephemeris was estimated. Figure 4 compares the frequency residuals from the inversions of the total-power spectra to those from the individual estimations described in section 3.

Simulations [*Hudson and Ostro*, 1990] show that image fidelity suffers if the global scattering law used in the inversion differs considerably from the actual law. A reasonable approach is to treat n as a free parameter and adopt the best value in a least squares sense. Our inversions show very little sensitivity to n unless we constrain the albedo distribution to be uniform, in which case we obtain values of n equal to (1.7, 1.4, 1.4) for the total power spectra of Europa, Ganymede, and Callisto, respectively. For SC spectra we obtain (1.7, 1.4, 1.3) and for OC spectra we obtain (1.8, 1.4, 1.6). These values differ insignificantly from weighted means of values estimated from fits to individual spectra (Table 8). For each of our nine unconstrained inversions, we adopted the value of n from the constrained inversion. Simulations also show that the fidelity of Doppler maps derived from radar data depends on the SNR,

which is not very high for our data, and on the sharpness of spectral features, which is rather low for these targets.

A spherical harmonic series of degree L contains $(L + 1)^2$ coefficients, and this number represents the number of independent resolution cells placed on the target's surface. The size of L is limited by the rotation phase coverage. The spherical harmonic series contains terms of the form $\cos(L\phi)$ and $\sin(L\phi)$, so L should be less than half the number of single-date spectra. We chose values of L equal to 5, 7, and 8 for Europa, Ganymede, and Callisto, corresponding to 36, 64, and 81 cells, respectively.

Generating the maps involved using singular value decomposition to invert the relevant matrices and determining the appropriate truncation level for the singular values [Press et al., 1986]. In this process one can neglect contributions corresponding to small singular values, decreasing noise sensitivity while discarding some of the underlying "true" map. For each satellite and each polarization, we performed several inversions in which additional noise, with the same variance as the receiver noise, was added to the spectra. We truncated the singular values until the resulting albedo maps appeared to be essentially independent of the noise realization, and we used this truncation level in our final inversions.

Figure 8 shows OC, SC, and total power (T = OC + SC) maps estimated from Arecibo spectra for Europa, Ganymede, and Callisto. The maps are necessarily "north-south ambiguous" because the subradar points are never more than a few degrees from the equator. Nonetheless, the maps permit tentative correlation of spectral features with surface features because the distribution of geologic terrains has negligible north-south symmetry. In Figure 8 the Doppler maps are shown as Lambert equal-area maps for leading-side ($\phi = 90°$) and trailing-side ($\phi = 270°$) projections to facilitate comparison with airbrush maps of the satellites in the same format. We discuss results for each satellite individually.

Callisto. The brightest feature in the 90° projections overlaps Valhalla, which is centered roughly 10° north of the equator. Other radar-bright areas appear roughly between 120° and 150° W longitude and between 30° and 60° N/S latitude. The northern one of these lies on the northern half of Asgard near the craters Burr and Sudri. The equatorial radar-dark spot near the same longitude corresponds to a nondescript region in the Voyager maps. Comparison of the SC and OC 90° maps suggests that μ_C is enhanced in the highest-albedo areas. (Evidence for a weak hemispheric asymmetry in μ_C was mentioned in section 5, on the basis of spectral features and disc-integrated estimates of $\mu_C(\phi)$.) In the 270° projection, the somewhat radar-bright equatorial feature corresponds to an area that contains the large, double-ringed crater Igaluk but is otherwise nondescript.

Ganymede. Prominent in the 90° maps is a very dark region centered roughly between 120° and 150° W longitude and at 30° N/S latitude. If it were at least in part a northern feature, it could fall in the center of Galileo Regio. Galileo Regio is optically dark, probably due to a relatively high silicate abundance in the surface material. Perrine Regio, centered near 50°W longitude and 30°N latitude, also is optically dark; it does not show up as a radar-dark feature, possibly because much of it is N/S ambiguous with optically bright areas in the southern hemisphere. In the 270° maps there are very bright features centered roughly between 210° and 240° W longitude and at 60° N/S latitude. Optically bright units in both hemispheres are candidates for the source(s) of the radar bright terrain(s).

Europa. The Europa data set has relatively sparse rotation phase coverage and very weak spectral features. Some of the spectra display a slight skewing or flattening relative to what

one would expect for a uniform sphere. The OC, SC, and T maps are similar. The 90° projection shows a dark equatorial region surrounded by bright regions between 30° and 60° N/S latitude. Voyager images of Europa's leading side show relatively dark markings at equatorial latitudes, so maybe we are seeing a correlation between optical and radar albedos like that seen for features on Ganymede and Callisto. Compared to the 90° projection, the 270° projection shows less contrast between equatorial and temperate latitudes. To the degree to which this difference is "real" it might be related to asymmetries seen between the leading and trailing sides in Voyager multispectral maps [McEwen, 1986; Nelson et al., 1986]. The polar regions appear dark, but the fidelity of the Doppler maps shown here is worst for the polar regions.

Figure 9 shows histograms for the satellites' OC, SC, and T albedo distributions derived from the Doppler maps. The histograms overlap each other. The brightest Callisto areas, including the feature identified with Valhalla, are at least as bright as the darkest Ganymede areas, e.g., the feature identified with Galileo Regio. Much of Ganymede is at least as bright as portions of Europa. The widths of the histograms increase from Callisto to Ganymede to Europa, in ratios (1 to 2 to 3.5) similar to those seen for $\hat{\sigma}_T$. We stress that because of the N/S ambiguity in Doppler maps constructed from echoes obtained near equatorial subradar latitude, the albedo estimated for any nonequatorial region will take on some value between the true albedos of the north and south conjugate regions. Therefore the true albedo distributions are likely to be wider than our histograms.

6. DISCUSSION

Figure 10 plots our estimates of the satellites' $\hat{\sigma}_T$ versus μ_C and illustrates how dramatically the radar properties of Europa, Ganymede, and Callisto differ from each other and from a "normal" target like the Moon. Europa is distinguished by the highest radar albedo measured for any planetary body. It is the most limb darkened of the icy Galilean satellites and also appears to have the broadest distribution of albedo. Callisto is the darkest of the three and has the narrowest albedo distribution. Ganymede, which is the "intermediate object" in terms of both the average albedo and the width of the albedo distribution, has a scattering law similar to Callisto's and a circular polarization ratio similar to Europa's.

Figure 10 illustrates the virtual absence of wavelength dependence seen between 3.5 and 13 cm. Echoes detected from all three satellites with Arecibo's 70-cm system during 1988-1990 (D. B. Campbell et al., unpublished results, 1992) yielded μ_C estimates that exceed unity and are consistent with the short-wavelength estimates. It thus seems reasonable to conjecture that the satellites' polarization properties are almost constant over a 20-to-1 wavelength range. According to coherent backscatter theory [Peters, 1992], the satellite regoliths look to the radar like a disordered random medium containing anisotropic scatterers. Wavelength independence in μ_C throughout the centimeter-to-meter regime would imply that the regoliths possess some sort of structural self-similarity at those scales. If so, then the scattering might arise less from individual pieces of ejecta and more from uncoordinated modulations in porosity (and hence refractive index) that occur randomly throughout "smoothly heterogeneous" regoliths [Ostro and Shoemaker, 1990].

The range spanned by the target-averaged values of $\hat{\sigma}_{OC}$ is three times greater than it is for μ_C (Figure 10), and albedo features are far more common than μ_C features. Thus both intersatellite and intrasatellite variations in albedo are much greater than the corresponding variations in μ_C. This result is
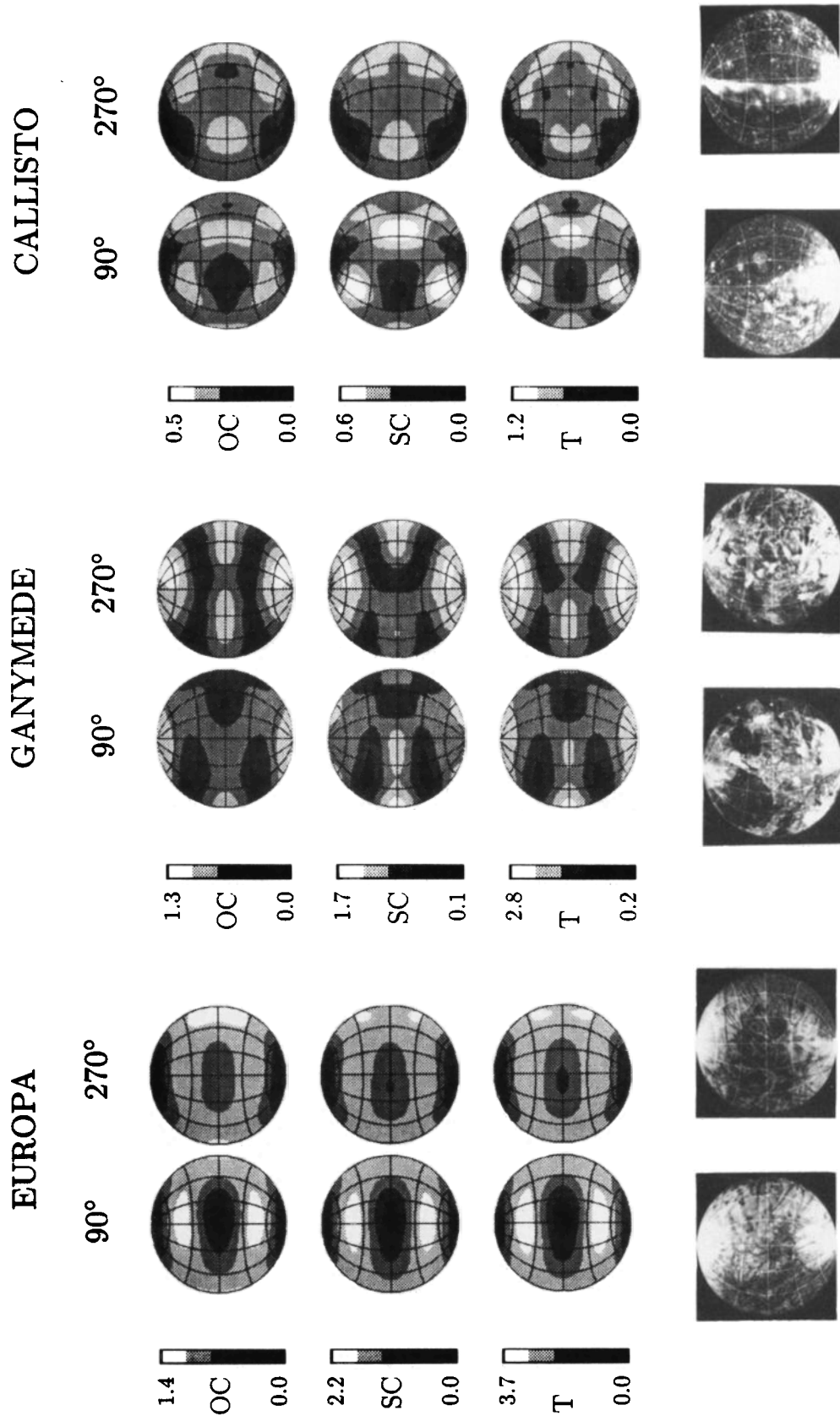
Fig. 8. OC, SC, and total power (T = OC + SC) Doppler maps of the icy Galilean satellites, estimated from Arecibo 13-cm single-date spectra as described in the text. The gray scales indicate radar albedo $\hat{\sigma}$. For a sphere with backscattering law $\sigma_0(\theta) = d\sigma/dA = \rho \cos^n\theta$, with ρ the normal-incidence albedo, $\hat{\sigma}$ satisfies the equation $\hat{\sigma} = 2\rho/(n+1)$. Our Doppler mapping solutions yield values of n for which $\hat{\sigma}/\rho$ is within 10% of 0.79. At the bottom are U. S. Geological Survey airbrush maps based on Voyager images; see Burns and Matthews [1986] for larger versions labeled with the names of geologic features. All the maps in this figure are Lambert equal-area projections. For each satellite, the left-hand and right-hand columns show leading-side ($\phi = 90°$) and trailing-side ($\phi = 270°$) projections, respectively, where ϕ is the west longitude of the central meridian. North is toward the top.
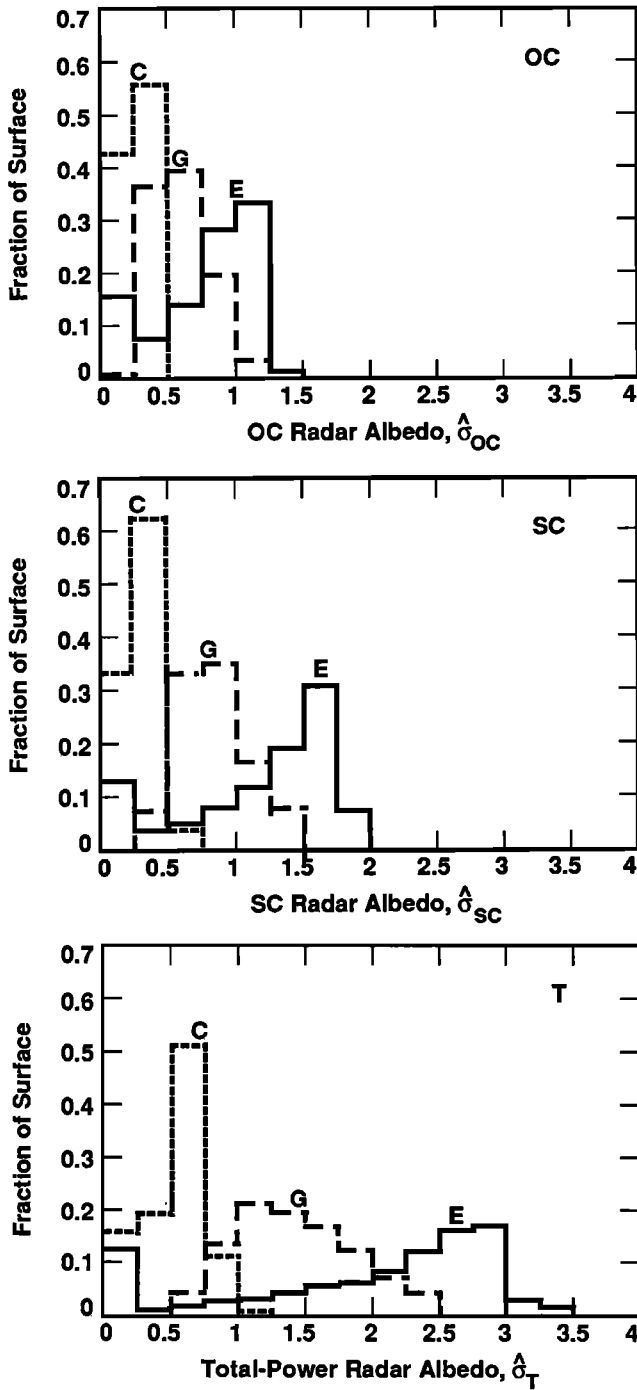
Fig. 9. Distributions of OC, SC, and total power (T) albedo on the satellite surfaces, derived from the Doppler mapping solutions. The horizontal positions of the letters E, G, and C correspond to the target-averaged values of disc-integrated measurements in Table 8.
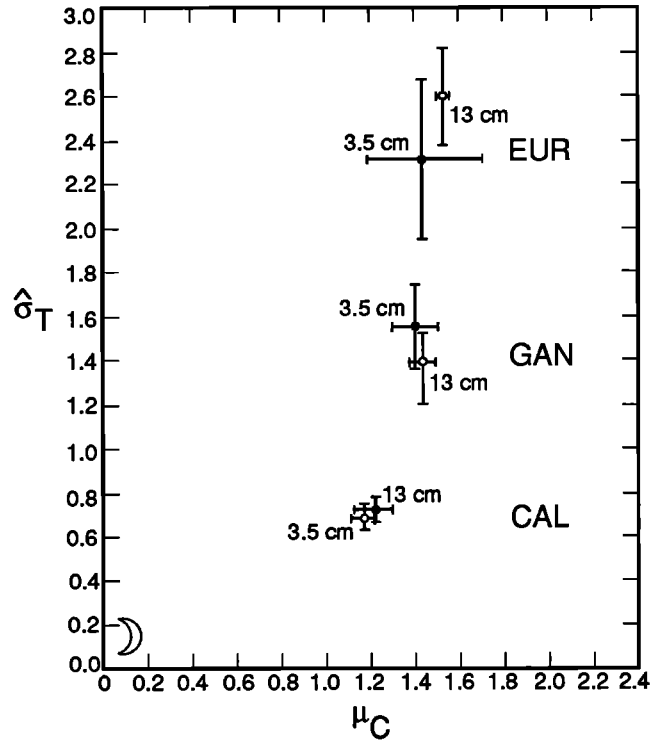
Fig. 10. Average values and rms dispersions of $\hat{\sigma}_T$ and μ_C for Europa, Ganymede, Callisto, and the Moon.

understandable in terms of coherent backscatter theory [*Peters*, 1992], which for a half-space of anisotropic scatterers predicts that increasing the ratio of the inelastic mean free path for absorption to the elastic mean free path for scattering from 2 to ∞ would increase the backscattered intensity by a factor of 2.6 and μ_C by a factor of only 1.2. In other words, we expect a much greater range in albedo than in polarization ratio. The absorption of ice increases dramatically as silicate abundance increases; this factor is likely to bear major responsibility for the distribution of radar albedo in the icy satellite system. Conversely, radar albedo might be a crude indicator of ice

purity, which might be lowest for the most ancient terrains and highest for terrains that have experienced relatively recent resurfacing.

The most prominent features evident in our spectra correspond to surface features whose scale is much smaller than hemispheric. For this reason, these features introduce little variation in the disc-integrated albedo as a function of rotation phase (Figure 5). We stress that the SNR of our spectra is barely high enough to support radar mapping, and that observations with a more sensitive radar might be expected to reveal variations in albedo (and perhaps in polarization ratio) not evident in our data. SNRs achievable with the upgraded Arecibo will be an order of magnitude greater than for the observations reported here. The next Jupiter opposition within the Arecibo declination window occurs in 1999. Meanwhile, radar observations with Goldstone and the Very Large Array can synthesize images free of any north/south ambiguity, permitting more definitive identification of radar features' source regions.

Detailed physical interpretation of the satellites' radar properties in terms of regolith characteristics is beyond the scope of this observational paper, but should be pursued now that a sound theoretical foundation is provided by the coherent backscatter literature. We expect that such efforts will provide useful insight into the connections between radar signature and surface age, regolith composition, and effects of endogenic and exogenic processes. (Research in this area might have ramifications outside planetary science: Europa, Ganymede, and Callisto can be thought of as laboratory samples for the study of weak localization at macroscopic wavelengths.) Of course, the Galileo mission holds the greatest promise for a significant advance in our understanding of these objects.

APPENDIX: ERRORS IN ESTIMATES OF RATIOS

(The notation in this appendix is not used elsewhere in this paper.) Suppose that x_1, x_2 are unbiased estimates of random variates X_1, X_2 obtained as linear functions of observations

contaminated by normally distributed errors with variances v_{11}, v_{22}, and covariance v_{12}. Defining $m = x_1/x_2$ as an estimate of $\mu = X_1/X_2$, with X_2 and x_2 nonzero, Fieller's theorem [Finney, 1964] sets upper and lower limits on μ:

$$m_U = [m - gv_{12}/v_{22} + Y]/(1 - g) \qquad (A1)$$

$$m_L = [m - gv_{12}/v_{22} - Y]/(1 - g) \qquad (A2)$$

where

$$Y = (t / x_2) [v_{11} - 2mv_{12} + m^2 v_{22} - g(v_{11} - v_{12}^2 / v_{22})]^{1/2} \qquad (A3)$$

$$g = t^2 v_{22}/x_2^2 \qquad (A4)$$

and t is Student's t statistic with v degrees of freedom at a specified significance level. For the observations reported here, v is so large that the distribution of t is nearly normal. By setting $t = 1$, we determine limits with the same probabalistic connotation as values one standard deviation from a parameter estimate. In other words, the probability that $m_L \leq \mu \leq m_U$ is 0.68. If $m = (m_L + m_U)/2$, we express the ratio estimate as $m \pm (m_L - m_U)/2$.

REFERENCES

Berge, G. L., and S. Gulkis, Earth-based radio observations of Jupiter: Millimeter to meter wavelengths, in *Jupiter*, edited by T. Gehrels, pp. 621-692, University of Arizona Press, Tucson, 1976.

Burns, J. A., Some background about satellites, in *Satellites*, edited by J. A. Burns and M. S. Matthews, pp. 1-38, University of Arizona Press, Tucson, 1986.

Burns, J. A., and M. S. Matthews (Eds.), *Satellites*, pp. 892-897, University of Arizona Press, Tucson, 1986.

Butler, B., D. O. Muhleman, A. Grossman, and M. Slade, Global radar mapping of Mars: Surface and subsurface (abstract), *Eos Trans. AGU*, 70, 1171, 1989.

Campbell, D. B., J. F. Chandler, G. H. Pettengill, and I. I. Shapiro, Galilean satellites of Jupiter: 12.6-cm radar observations, *Science*, 196, 650-653, 1977.

Campbell, D. B., J. F. Chandler, S. J. Ostro, G. H. Pettengill, and I. I. Shapiro, Galilean satellites: 1976 radar results, *Icarus*, 34, 254-267, 1978.

Eshleman, V. R., Mode decoupling during retrorefraction as an explanation for bizarre radar echoes from icy moons, *Nature*, 319, 755-757, 1986a.

Eshleman, V. R., Radar glory from buried craters on icy moons, *Science*, 234, 587-590, 1986b.

Finney, D. J., *Statistical Method in Biological Assay*, 2nd ed., p. 24, Hafner, New York, 1964.

Goldstein, R. M., and R. R. Green, Ganymede: Radar surface characteristics, *Science*, 207, 179-180, 1980.

Goldstein, R. M., and G. A. Morris, Ganymede: Observations by radar, *Science*, 188, 1211-1212, 1975.

Hagfors, T., T. Gold, and M. Ierkic, Refraction scattering as origin of the anomalous radar returns of Jupiter's satellites, *Nature*, 315, 637-640, 1985.

Hapke, B., Coherent backscatter and the radar characteristics of outer planet satellites, *Icarus*, 88, 407-417, 1990.

Hapke, B., and D. Blewett, Coherent backscatter model for the unusual radar reflectivity of icy satellites, *Nature*, 352, 46-47, 1991.

Harmon, J. K., and M. A. Slade, An S-band radar anomaly at the north pole of Mercury (abstract), *Bull. Am. Astron. Soc.*, 23, 1197, 1991.

Hudson, R. S., and S. J. Ostro, Doppler radar imaging of spherical planetary surfaces, *J. Geophys. Res.*, 95(B7), 10,947-10,963, 1990.

John, S., Localization of light, *Phys. Today*, 44, 32-40, 1991.

Lieske, J. H., Improved ephemerides of the Galilean Satellites, *Astron. Astrophys.*, 82, 340-348, 1980.

MacKintosh, F. C., and S. John, Coherent backscattering of light in the presence of time-reversal-noninvariant and parity-nonconserving media, *Phys. Rev. B*, 37, 1884-1897, 1988.

MacKintosh, F. C., and S. John, Diffusing-wave spectroscopy and multiple scattering of light in correlated random media, *Phys. Rev. B*, 40, 2383-2406, 1989.

MacKintosh, F. C., J. X. Zhu, D. J. Pine, and D. A. Weitz, Polarization memory of multiply scattered light, *Phys. Rev. B*, 40, 9342-9345, 1989.

McEwen, A. S., Exogenic and endogenic color patterns on Europa, *J. Geophys Res.*, 91, 8077-8097, 1986.

McKinnon, W. B., and E. M. Parmentier, Ganymede and Callisto, in *Satellites*, edited by J. A. Burns and M. S. Matthews, pp. 718-763, University of Arizona Press, Tucson, 1986.

Muhleman, D. O., A. W. Grossman, B. J. Butler, and M. A. Slade, Radar reflectivity of Titan, *Science*, 248, 975-980, 1990.

Muhleman, D. O., B. J. Butler, A. W. Grossman, and M. A. Slade, Radar images of Mars, *Science*, 253, 1508-1513, 1991.

Nelson, M. L., T. B. McCord, R. N. Clark, T. V. Johnson, D. L. Matson, J. A. Mosher, and L. A. Soderblom, Europa: Characterization and interpretation of global spectral surface units, *Icarus*, 65, 129-151, 1986.

Ostro, S. J., Radar properties of Europa, Ganymede, and Callisto, in *Satellites of Jupiter*, edited by D. Morrison, pp. 213-236, University of Arizona Press, Tucson, 1982.

Ostro, S. J., and E. M. Shoemaker, The extraordinary radar echoes from Europa, Ganymede, and Callisto: A geological perspective, *Icarus*, 85, 335-345, 1990.

Ostro, S. J., D. B. Campbell, G. H. Pettengill, and I. I. Shapiro, Radar observations of the icy Galilean satellites, *Icarus*, 44, 431-440, 1980.

Peters, K. J., The coherent backscatter effect: A vector formulation accounting for polarization and absorption effects and small or large scatterers, *Phys. Rev. B*, 46, 801-812, 1992.

Press, W. H., B. P. Flannery, S. A. Teukolsky, and W. T. Vetterling, *Numerical Recipes*, 818 pp., Cambridge University Press, New York, 1986.

Standish, E. M., The observational basis for JPL's DE200, the planetary ephemerides of the Astronomical Almanac, *Astron. Astrophys.*, 233, 252-271, 1990.

Slade, M. A., B. Butler, D. Muhleman, and R. Jurgens, Mercury Goldstone/VLA radar: Part I (abstract), *Bull. Am. Astron. Soc.*, 23, 1197, 1991.

Tiuri, M. E., Radio astronomy receivers, *IEEE Trans. Antennas Propag.*, AP-12, 930-938, 1964.

Wolf, P., and G. Maret, Weak localization and coherent backscattering of photons in disordered media, *Phys. Rev. Lett.*, 55, 2696-2699, 1985.

D. B. Campbell, National Astronomy and Ionosphere Center, Cornell University, Ithaca, NY 14853.

J. F. Chandler and I. I. Shapiro, Harvard-Smithsonian Center for Astrophysics, 60 Garden St., Cambridge, MA 02138.

R. M. Goldstein, S. J. Ostro, K. D. Rosema, E. M. Standish, R. Winkler, and D. K. Yeomans, Jet Propulsion Laboratory, California Institute of Technology, Pasadena, CA 91109.

R. S. Hudson, School of Electrical Engineering and Computer Science,Washington State University, Pullman, WA 99164.

R. A. Simpson, Center for Radar Astronomy, Stanford University, Stanford, CA 94305.

R. Velez, National Astronomy and Ionosphere Center, Box 995, Arecibo, PR 00613.